The Dissertation Committee for Youngkyu Lee Certifies that this is the approved version of the following dissertation:

Light Manipulation through Periodic Plasmonic Corrugations

Committee:

Xiaojing Zhang, Supervisor

Andrea Alù

Mikhail Belkin

Zheng Wang

Hsin-Chih (Tim) Yeh

Light Manipulation through Periodic Plasmonic Corrugations

by

Youngkyu Lee, B.S.E; M.S.E.

Dissertation

Presented to the Faculty of the Graduate School of

The University of Texas at Austin

in Partial Fulfillment

of the Requirements

for the Degree of

Doctor of Philosophy

The University of Texas at Austin

May 2014

Acknowledgements

There are many people to whom I would like to express my deepest appreciation for their professional guidance, leading to the successful completion of this dissertation. First of all, I would like to gratefully and sincerely thank Dr. Xiaojing Zhang for his guidance, understanding, patience, and most importantly, his supports during my graduate studies at the University of Texas at Austin. He helped me achieve a well-rounded experience required for my long-term career goals. Without his guidance, I would never complete meaningful studies for my doctoral degree. Also I would like sincerely thank to Dr. Andrea Alù for his insightful advices and theoretical guidance. Without his guidance, there would be no research that I can carry out and develop further. All my gratitude goes also to Dr. Hsin-Chih Yeh, Dr. Mikhail Belkin, and Dr. Zheng Wang who sit on my dissertation committee and provide insightful advices on my dissertation research.

There are many other people who contributed to this dissertation but, but most of all I would never forget supports from my family. Mom and Dad, you are the smartest people that I have met in my life and your encouragements have meant a lot to me to power through hiccups in long graduate student life.

Youngkyu Lee

The University of Texas at Austin
May 2014

Light Manipulation through Periodic Plasmonic Corrugations

Youngkyu Lee, Ph. D.

The University of Texas at Austin, 2014

Supervisor: Xiaojing Zhang

Collective oscillations of free electrons localized in a small volume have drawn a lot of attention for the past decades. These so-called plasmons have special optical properties that can be used in many applications ranging from optical modulators to sensing of small quantities of molecules. Large numbers of extensive plasmonic applications are being based on the capability of light manipulation proposed by the periodic nanostructure and its optical response. By controlling over the way in which plasmonic modes interact with incident radiation, periodic corrugation opens up the possibility of developing new and exciting photonic devices.

The goal of doctoral research presented herein is to investigate at a fundamental level of several corrugated metallic structures which may offer effective control of the optical response by coupling radiation to plasmonic modes. By controlling morphologies and material compositions, sophisticatedly engineered nanostructure may allow the coupling of electromagnetic waves into desired spectral/spatial modes in a way that an effective tuning of macroscopic optical properties in desired domain can be achieved. This dissertation is dedicated to answer the following question, if and how one can manipulate the optical responses by use of different nanostructures and various materials.

Based on devised analytical models proposed for various corrugated nanostructures, we show that I. spatial and II. spectral manipulation of light can be realized. Specifically, we investigate how the grating array interacts with light. To understand those periodic nanostructures showing inherently dispersive nature, firstly the diffraction of light and accompanying effects are studied with the analytical models and numerical simulation. On this basis, we show the optical response is readily tunable, and efficiently controlled by the morphology and dielectric property of the corrugations. The outline of doctoral research is broadly categorized into (1) theoretical considerations on the topic of plasmonics, (2) specific insight in the analytical model of the various nanostructures, and (3) investigation of the plasmonic properties of the fabricated structures. Lastly, the discussion of outlook to possibilities and future experiments will close the dissertation.

Table of Contents

List of Tables

List of Figures

Chapter: 1 Introduction

1.1 LIGHT AND PERIODIC MATERIALS

Even before the advent of the Maxwell's dynamical theory of electromagnetic field [1], the concept of wave interactions with a periodic medium has been a classical subject in science history. In many research areas ranging from acoustics to optics, the modified wave function by periodic media has been actively studied [2-18] in the sense of controlling wave diffractions into spectral/spatial orders [4, 5, 7-9, 13, 15] instead of being scattered over the space as on bulk surface. Especially, the generic term gratings; they have been widely applied to the structure producing a microscopic variation of the phase in turn modifying the amplitude transmittance/reflectance of waves. Aiming at the effective tuning of wave interference, a grating has been frequently used for manipulating lights especially when monochromatic light is involved or when spectral separation is required [4, 9]. Among many grating applications, diffraction gratings have been a famous tool in the wide scope of spectroscopic applications and in many domains of physics including the solid-state physics, X-ray instrumentation, lasers, optical communication, and astronomy.

Other than typical wave diffraction, one unique wave interaction associated with periodic gratings so called "Wood's anomalies" [19] was reported in 1902. Since unexpected band suppression that appears in allowable spectrum of gratings could not be understood by ordinary grating theory of that time, sharp intensity variation in spectrum resolved by diffraction gratings has been termed "grating anomalies [19]." The phenomena, grating anomalies, have constituted a topic of many researches for many

years; and important scientific findings have been made [20-23] with the development of relevant theoretical treatments [20-25].

My doctoral research that will be presented herein lies at the basis of grating theories [19-23, 25-27] including typical diffraction theory and anomalous modal reconfiguration through wave coupling into surface and/or guided waves. Extending from those pioneering works, we further investigate the new capability of periodic corrugations that may show effective and tunable spatial/spectral molding of light. Before moving forward to the presentation of our studies, it would be worth to review pioneering works [19-23, 25] relevant to the light interaction with periodic corrugations, since analogues in grating theories are frequently referred in this dissertation. With this mind, this chapter will be devoted to overviewing the grating theories from which one may gain fundamental understandings of our researches.

1.2 General Property of Grating Diffraction: Rayleigh Wavelength

Since the first reports of grating diffraction [6], the study of light interaction with the periodicity and frequency of waves became important topic for understanding the nature of light. As a consequence of the coherent wave interference imposed by periodic corrugated structure, the wave diffraction offers reconfigurable spatial/spectral orders of light so that important applications such as color filters and spectroscopy could be developed. Prime property of diffraction gratings is to create the discrete diffraction orders in various domain. By having spatially modulated geometry forming a periodic array, the resultant wave response implies inherently discrete nature. Although the complex theoretical treatments [5, 28, 29] may be required for accurate analysis, general behavior of gratings can be well comprehended by simpler analytical form as in

Huygens's construction which was first done by Fresnel, considering it as a collection of reflecting/transmitting elements separated by a wavelength-comparable distance.

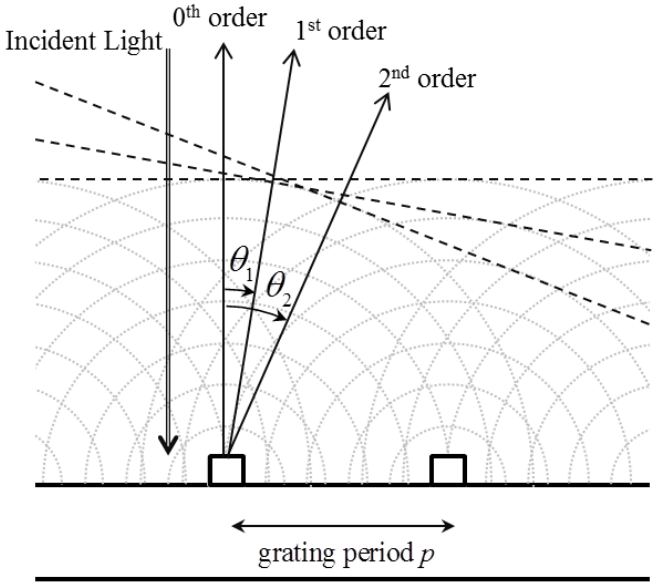

Figure 1-1. Diffraction by gratings: monochromatic light is incident normally on gratings and diffracted across spatial orders ruled by grating periodicity p.

The fundamental equation governing the performance of a diffraction grating is a grating equation giving the order n, wavelength λ, periodicity p, angle of incidence ϕ, and angle of diffraction θ which follows $n\lambda = p\left(\sin\theta \pm \sin\phi\right)$. For a choice of the reflection gratings and more simplified example where normal incident light ($\phi = 0°$) is considered, periodic gratings diffract the incident monochromatic light into several discrete directions as depicted in Figure 1-1. Following the Huygens's construction, we can picture each grating corrugation as being a tiny source of light, combined to form a

diffracted wavefront. The use of a grating depends on that there exists a unique set of discrete angles along which, for a given spacing p between corrugations, the diffracted light from each facet is in phase with the light diffracted from any other facet, so they combine constructively. These relationships are expressed by the simpler grating equation $p \cdot \sin\theta = m\pi$, which holds for general grating diffractions as long as the corrugations are smaller than the wavelength of light. Several different treatments can be used to analyze the diffraction of light by gratings (or sometimes referred to as spatially modulated media). The common methodologies are the coupled-wave approach [27, 30-34] and the modal analysis [35-42]. Both approaches enable the formulation of wave interaction with gratings in rigorous manner so that exact wave behavior can be estimated. Albeit, these methodologies are rather difficult and time consuming work due to the complex numerical calculations are involved; however, proper approximation may be made in order to gain comprehensive understandings on wave diffraction on gratings.

1.3 GRATING ANOMALIES

It was discovered by R. W. Wood [19] that anomalous sharp variation in either transmission or reflection spectra, which is unable to be explained by conventional diffraction theory of that time, can arise from metal gratings. Since its first discovery, grating anomalies have drawn wide attention from many researchers including U. Fano [20] who offered theoretical breakthrough on these. There are two primary reasons that the grating anomalies had gained a renewed interest from researchers after 60 years of its discovery. One is the increasingly widespread use of gratings in applications that has become of significant importance in space research and in solid state physics. In order to minimize the anomalous grating effects which might give rise to an inaccurate result, better understandings on unexpected grating phenomena had to be studied. A second

reason for the interest in grating anomalies was the fact those anomalies could be explained in terms of surface wave modes in metal. The widely accepted mechanism of grating anomalies, as pointed out by several antecedents [19-23, 25, 26], is based on two distinguishable treatments: the one with Rayleigh's conjecture [22, 26] and the one with resonant modes of guided wave propagating tangentially along periodic corrugations. In this section, general description and treatment on grating anomalies are presented.

1.3.1 Rayleigh's conjecture

The first theoretical treatment was made by Rayleigh [22, 26] in 1907. This theory involved an expansion of the electromagnetic field in terms of outgoing waves which predicted a singularity at certain specified wave lengths. Such Rayleigh's conjecture on the dynamic theory of the grating [22, 26] can be formulated as:

$$k_n^{\|} - k_0^{\|} = 2n\pi / p, \tag{1-1}$$

where $k_n^{\|}$ is a wavenumber of order n grating diffraction along the structure, $k_0^{\|} = k_0 \sin(\theta)$ is a wavenumber of impinging light along the structure with an angle of incidence θ, and p is a periodicity of structure. Since the absence or emergence of spatial modes associated with the scatterings of order n diffraction, in theory, corresponds to the fact that observable light diffraction does not propagate out from the structure ($\mathrm{Re}\left[k_n^{\perp}\right] = 0$, where $k_n^{\perp}$ is a wavenumber of order n diffraction normal to grating surface), Rayleigh deduced a simple relation that the wavelengths of spectrum generating the passing-off of diffracted order can be derived as:

$$n\lambda / p = -\sin(\theta) \pm 1, \; n = \pm 1, \pm 2, \pm 3... \tag{1-2}$$

, where λ is the frequency of operation. Despite its poor accuracy, Rayleigh could explain the Wood's anomalous observation using the Equation (1-2). Rayleigh's theory was useful in predicting the position of the wavelengths but not their shape or intensity.

1.3.2 Resonant Grating Anomalies

Although the Rayleigh conjecture predicts the location of the sharp anomaly, it was yet unable to explain the diffusive nature of anomalous diffraction experimentally witnessed by Wood [19]. Being based on the Wood's experimental observations, U. Fano made an insightful conclusion and claimed that the grating anomalies can be distinguished in two different kinds:

- Passing-off of higher diffraction order (a sharp anomaly).
- Forced resonance, associated with diffusive spectrum.

The major discrepancy between the theoretical predictions by Rayleigh and the experimental data provided by Wood is the fact that the diffuse anomaly is rather related to the "leaky waves supportable by the grating", which is also confirmed by Hessel and Oliner [21]. Although these two authors used numerical tools in order to calculate the location and shape of the anomalies; however, their analysis model used was based on the knowledge a priori of the electromagnetic impedance (ratio of the tangential components of the electric/magnetic fields) on a straight line located above the grating grooves, which would face some cases that could not be clearly explained. Nevertheless, they were able to explain some properties experimentally known, such as the possibility of anomalies for p-polarized light with very deep gratings, or the reluctance of anomalies to merge.

1.3.3 Guided Waves on Surface

U. Fano in [20] introduced a method of successive approximations to explain the anomalous interference effects and gave an explanation of the anomalies in terms of

superficial waves excited on the metallic grating surface. These superficial waves can be considered as quasi stationary superficial waves obtained mathematically by Sommerfeld (Sommerfeld's waves). In connection with this problem, U. Fano in [20] told that the problem of propagation of light traveling along 1D diffraction grating is analogous to the problem of the radiation by an antenna near the surface of a conducting body. The similar point of view on the origin of Wood's anomalies was proposed in [5]. Contrary to customary multiple scattering procedures [7] the authors of [5] presented a theory of Wood's anomalies which is based on guided wave approach. They showed that there are two types of the anomalies: a Rayleigh type of the ones which is characterized by an abrupt intensity modulation of the diffraction orders at appearance and fading of the new spectral orders and a resonant type of the anomalies corresponding to the resonances of guided complex waves of the gratings. It is worth mentioning that these two types of the anomalies can occur either separately or even simultaneously.

1.4 SCOPE OF DISSERTATION

The scope of this dissertation includes our answer to the question, if and how one can manipulate the optical responses by use of different nanostructures and various materials being based on the light interactions with periodic structures. The thesis consists of two main parts. The first part, spatial manipulation of light, covers our effort to realize a compact light beaming mechanism using periodic nanostructures. Specifically, it includes the analytical solution to the edge scatterings derived from the rigorous perturbation theories and experimental demonstration.

First, low-profile plasmonic gratings are designed to achieve the efficient directional beaming from the surface. Being based on the analytical study, designed

plasmonic gratings can be effectively couples the surface plasmonic waves into leaky waves propagating in the desired spatial order. The measurements show that the improvement of directivity can be realized by optimizing the design parameters including grating period and distance between the slit and gratings. It is also shown that the directivity can be further improved with unidirectional coupling of surface plasmonic waves utilizing the multi-modal propagation of a slit.

Second, tunable directional radiation is explored to further extend the manipulation of light in spatial order. For tunability, it is found that the direction of light can be controlled through tailoring the bulk index of dielectric medium around the plasmonic gratings. We integrate the microfluidic system to provide the intended controls of medium index so that dynamic tuning of radiation direction can be achieved.

In the following part, the mechanism of spectral manipulation of light is studied. Being inspired by the Wood's grating anomalies which may be due in part to the guided modes on gratings, we utilize the well-defined waveguide geometries that enable the formation of horizontal guided modes for forming bandgap responses. We demonstrate that the optical transmission spectrum is controllable through coupled resonance mode and/or impedance matching condition across the horizontal waveguides hence capable to create omnidirectional bandgap or effective light transmission conditions. Relevant applications utilizing the property of bandgap response are also presented in this part. First, to offer a solid mechanism of omnidirectional reflection phenomenon for the grating structure, an analytical models based on the transmission-line approach are investigated for the plasmonic geometry having a horizontal waveguide structure across an array of slits; and the analytical models are then compared to numerical simulations. The derived analytical model show good agreement for the effective band suppression of

transmitted light for omnidirectional incident angle. The experimental demonstration for such bandgap response is also presented in this part.

Secondly, it is also predicted that the light transmitted through the proposed geometry is highly dependent on the modal impedance matching conditions of slit array compensated by the horizontal waveguide geometry. By tailoring the impedance matching conditions, the light transmission through the proposed geometry can be effectively suppressed or even tuned. Such tunable transmission of light are experimentally demonstrated and compared with the theory.

Chapter 2: Theoretical Background

This chapter will present the theoretical background which is necessary to understand theoretical analyses and experimental results introduced in this dissertation. Specifically, general theoretical considerations and theoretical treatments solving geometry-related plasmonic problems are presented.

2.1 SURFACE WAVES

The use of surface waves referred in many articles [21, 23-25, 27, 30, 32-34] to explain Wood's anomalies leads to investigating surface wave phenomena in metals in more depth in their general theories and in their specific application to the problem relevant to grating anomalies. As Sommerfeld [43, 44] showed that an electromagnetic wave could propagate at the boundary between two dielectric media, a solution to bound surface wave of the transverse magnetic (TM) wave propagation could be easily formulated form the Maxwell's equation to solve surface wave problem. One interesting property of a surface wave is its locality that its fields decay fast away from the surface interface and as such dissipate along the wave propagation. In a metal the oscillating longitudinal field can interact with the conduction electrons which in turn oscillate in the same direction. The essentially free conduction electrons and the lattice ions constitute a plasma in the metal. The conduction electron oscillation brought about by the surface wave can be interpreted as a wave of charge oscillations, or more exactly, as a surface plasmonic wave. Another interesting property of this surface wave is that its phase velocity is less than the speed of light. This directly corresponds to that an incident plane wave cannot excite the surface wave because momentum and energy cannot be simultaneously conserved at the boundary. Exceptions can be given when the surface is

not perfectly smooth or when multiple diffractions arise from a small geometry that able to create multiple momenta matched to momentum of surface wave.

2.2 THEORETICAL TREATMENTS ON PLASMONICS

In the vibrant field of nano meter scale geometry where the light interaction with matters is comparable to or smaller than the wavelength of operation, the process of plasmonics starts governing the macroscopic optical property. The fundamental of such plasmonic process is based on the interaction of the electromagnetic radiations with the conduction electrons in metal. Especially, the general term plasmons refer to electromagnetic waves formed at the interface between a metal and a dielectric medium and have origin from the coupling of the electromagnetic field with electron-plasma density oscillations in metal geometry. Since plasmonic waves are the localized solutions of Maxwell's equations being ruled by many factors including metal geometry, dielectric properties of matters, and wavelength of operation, many theoretical treatment for analyzing plasmonic waves on various geometries have been introduced. In this chapter, general theoretical considerations and treatments on plasmonics that would help understand the fundamental of plasmonic process will be presented.

2.2.1 Mie and Gans Solution

Relative simplicity and versatility are the advantages of the classical Mie theory suggested by Gustav Mie in 1908 [45], which describe the mechanism for the absorption of light by small metal particles by solving Maxwell's equations. The theory is based on the assumptions that while the electromagnetic field interacts with the particle an induced charge separation on the particle's surface succeed. This charge separation is a cause for

an occurring restoring force. It has been shown that such absorption of light in the ultra-violet and visible wavelengths by metallic particles is sensitive to many geometrical as well as environmental factors. Solving Maxwell's equations lead to a relationship for the extinction cross-section for metallic nanoparticles

$$\sigma_{extinction} = \sigma_{absorption} + \sigma_{scattering} \qquad (2.1)$$

,where $\sigma_{extinction}$, $\sigma_{absorption}$, $\sigma_{scattering}$ are the extinction, absorption, and scattering cross section of a particle, respectively. Although the processes of absorption and scattering are simultaneously occurring for impinging electromagnetic fields, the equation (2.1) can be significantly simplified when the small particle approximation (radius of particle $r << \lambda$) is applied. This approximation directly corresponds to the dominant effect of absorption for extinction; but it has to be noted that the extinction cross section relevant to absorption also consists of real and imaginary values which are associated with scatterings and ohmic losses of electromagnetic energy, respectively. Taking into account of complex dielectric constant of metal $\varepsilon_{\mathrm{M}}(\omega) = \varepsilon_{\mathrm{M}}^{'}(\omega) + i\varepsilon_{\mathrm{M}}^{''}(\omega)$, Mie [45] calculated the extinction cross section $\sigma_{extinction}$ as following:

$$\mathrm{Re}\left[\sigma_{extinction}\right] = 12\frac{\omega\pi}{c}\varepsilon_0^{1.5} r^3 \frac{\varepsilon_{\mathrm{M}}^{''}(\omega)}{\left[\varepsilon_{\mathrm{M}}^{'}(\omega) + 2\varepsilon_0\right]^2 + \varepsilon_{\mathrm{M}}^{''}(\omega)^2} \qquad (2.2)$$

, where ε_0 is the isotropic dielectric constant of surrounding medium where the small Mie scatter is embedded in. This formula predicts a resonant peak when $\varepsilon_0 = -0.5\varepsilon_{\mathrm{M}}^{'}(\omega)$. The Mie's solution to the extinction cross section of small, metallic particie had provided comprehensive knowledge on understanding significant optical scattering phenomenon from subwavelength-sized particles. Following the Mie's solution, in 1912 Richard Gans [46] presented his modification of the Mie theory, which

extended the expression for the extinction cross section by including the factor of depolarization imposed by morphology of particle. With this expression the calculation of the resonance for rod-like nanoparticles could be achieved. Since oscillations induce a charge separation and thus a localized plasmon resonance in the nanoparticle, the extinction cross section should include depolarization factors P_k which can be described as following:

$$\mathrm{Re}\left[\sigma_{extinction}\right] \cong \sum_k \frac{\varepsilon_{\mathrm{M}}^{"}(\omega)/P_k^2}{\left[\varepsilon_{\mathrm{M}}^{'}(\omega)+\frac{1-P_k}{P_k}\varepsilon_0\right]^2+\varepsilon_{\mathrm{M}}^{"}(\omega)^2} \qquad (2.3)$$

, where depolarization factor P_k is determined by physical morphology of particle. This modification by Gans [46] predicts the fact that multiple plasmonic modes can exist depending on the shape of particle and the total extinction cross section of the particle is proportional to the summation of those induced by multiple plasmonic modes.

2.2.2 Drude Model

Electromagnetic properties of material can be explained as the classical physical oscillation model. One important physical model to describe material dispersion is the Drude model presented in 1900 by German physicist, Paul Drude. The Drude model takes a macroscopic view of charge carrier motion, using a simple equation of motion and deriving the material permittivity. In this model, metals are characterized as cloud of free electron that are not bound to a particular atomic nucleus but are free to move within the metal lattice. The model also includes frictional damping that describes the resistance to movement felt by the electrons. This damping arises from collisions within the lattice between the moving electrons and the positive, stationary ions (metal nucleuses).

Although the Drude model does not take into account electron-electron interactions, it in general provides an accurate prediction comparing to the measured data [47], particularly for the noble metals [47-49], in certain frequency ranges. Being based on such free electron model where electrons move freely in between independent collision, the dispersion of metal can be described by following equation:

$$\varepsilon(\omega) = 1 - \frac{\omega_p^2}{\omega^2 - i\omega\Gamma_p} \qquad (2\text{-}4)$$

, where ω_p is the plasma frequency of metal and Γ_p is the damping rate connecting the Fermi velocity and the electron mean free path between collisions. More rigorous form of Drude model is used when a background interband contribution to the permittivity is considered.

$$\varepsilon(\omega) = \varepsilon_\infty - \frac{\omega_p^2}{\omega^2 - i\omega\Gamma_p} \qquad (2\text{-}5)$$

By taking account for the electron transition from different bands (ionic background of metal ε_∞), the more accurate surface plasmon resonance in metallic nanoparticles or complex geometry can be captured. The unique dielectric function of metal described by the Drude model can be clearly seen if Γ_p is neglected in the Equation (2.4). For the case where the frequency ω is higher than the plasma frequency ω_p, $\varepsilon(\omega)$ is positive and the dielectric property allows the propagation of electromagnetic waves inside the medium. In contrast, the electromagnetic waves exponentially decay due the negative permittivity. This property corresponds to the physical phenomenon that most metals are highly reflective for lights in visible spectrum. Since the value of plasma frequency ω_p varies for different metals [47], which in

general lies in the ultra-violet spectrum, an impinging light with $\omega < \omega_p$ reflects on metal surface due to the significant mismatch of wave propagation impedance.

Throughout this dissertation, treatments based on Drude model are used for the analysis of plasmonic geometry with analytical solution and numerical simulations. Although some discrepancy in between the experimental data and values expected from Drude model [50] is reported for some noble metals including gold especially in the visible spectrum, we will use silver as a basis of plasmonic geometry since its physical dielectric property [47] well agrees with Drude model.

2.2.3 Surface Plasmons

The treatment based on Drude model has been concerned with bulk oscillations of charge in infinite medium. But the situation would be rather different for the case where the medium has a boundary. For such case, we must account for what happens at the interface between two media having different dielectric properties when an electromagnetic disturbance passes from one medium into the other. This analysis is a classical boundary value problem in electromagnetic (EM) theory. We consider a semi-infinite conductor of dielectric constant ε_{M}, bounded by a vacuum as in Figure 2-1, that we can formulate the solution for an electromagnetic wave propagating along the interface; where, for simplicity we take the propagation vector, κ , along the x-axis. The electric fields must satisfy the wave equations

$$\nabla^2 \overline{\mathrm{E}} - \frac{1}{c^2}\frac{\partial^2 \overline{\mathrm{E}}}{\partial t^2} = 0, \quad \mathrm{z} > 0 \qquad (2\text{-}6)$$

$$\nabla^2 \overline{\mathrm{E}} - \frac{\varepsilon_{\mathrm{M}}}{c^2}\frac{\partial^2 \overline{\mathrm{E}}}{\partial t^2} = 0, \quad \mathrm{z} < 0 \qquad (2\text{-}7)$$

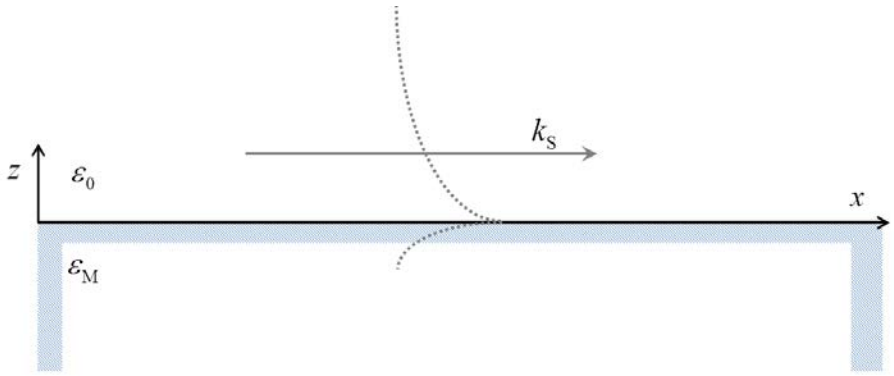

Figure 2-1: Boundary value problem for a surface wave formed at interface in between semi-infinite metal (ε_M) and vacuum (ε_0). κ is a wavenumber of surface wave propagating along the interface.

Retardation effects are automatically accounted for by the timedependent terms. We find that the solutions to Equations (2-5) and (2-7) have the following form:

$$\overline{\mathrm{E}} = e^{i(\kappa x-\omega t)} \begin{cases} \overline{\mathrm{A}}\, \mathrm{e}^{-k_{vac} z}, & \mathrm{z} > 0 \\ \overline{\mathrm{B}}\, \mathrm{e}^{-k_S z}, & \mathrm{z} < 0 \end{cases} \qquad (2\text{-}7)$$

, where $k_{vac} = \left(\kappa^2 - \omega^2/c^2\right)^{0.5}$ and $k_{vac} = \left(\kappa^2 - \varepsilon_M\, \omega^2/c^2\right)^{0.5}$. The media, exclusive of the boundary, are homogeneous and charge-free and we may write as $\nabla \times \overline{\mathrm{E}} = 0$ from which we have $i\kappa \mathrm{A}_x - k_{vac}\mathrm{A}_z = 0$, and $i\kappa \mathrm{B}_x - k_S \mathrm{B}_z = 0$. Since we consider the case where no free charges are present, the normal component of the displacement field $\overline{\mathrm{D}}$ is continuous across the boundary. Under such circumstance, we obtain

$$\begin{aligned} \mathrm{A}_x &= \mathrm{B}_x \\ \mathrm{A}_z &= \varepsilon B_z \end{aligned} \qquad (2\text{-}8)$$

The sets of solution that satisfy the Equation (2-7) and Equation (2-8), and the field continuity of magnetic potential yields a non-zero solution for the possible surface waves as following:

$$\begin{vmatrix} k_{vac} & k_{\mathrm{S}} \\ 1 & -\varepsilon_{\mathrm{M}} \end{vmatrix} = 0 \qquad (2\text{-}9)$$

Based on the Equation (2-9), we can obtain the dispersion relation for the surface wave $\kappa = \omega/c\left[\varepsilon_{\mathrm{M}}/\left(\varepsilon_{\mathrm{M}}+1\right)\right]^{0.5}$. This is a general property of a transverse magnetic (TM) electromagnetic wave supported at the metal and dielectric interface as seen in Figure 2-1. Because the z-dependence of a surface wave is exponentially decaying away from the interface, the wave is in general referred to localized waves being bound to limited volume along z. We may consider those bound surface waves propagating along the interface as guided waves propagating with the wavenumber κ. Other modes such as the transverse electric (TE) and transverse electromagnetic (TEM) waves do not yield non-singular solutions for a given geometry, so that the TM wave is the only possible solution for this case. This TM mode is the same as the one postulated by Sommerfeld [44] for a wave propagating at an earth-air inter face and it is also known as the Sommerfeld surface wave.

I. SPATIAL MANIPULATION OF LIGHT

In this part, we present our study on the spatial manipulation of light by use of different nanostructures. Specifically in chapter 3, we show that efficient directional beaming can be realized by use of planar nanostructure which is properly designed for efficient plasmonic diffractions into directional beaming. Following the findings described in chapter 3, we further experimentally demonstrate that directional beaming can be tuned to arbitrary direction upon the presence of control medium around a beaming device.

Chapter 3: Efficient directional beaming using surface-plasmon diffraction gratings

This chapter contains studies on efficient directional beaming from a small aperture aided by surface-plasmon diffraction gratings. In this study, we experimentally demonstrate efficient optical directional beaming using an array of subwavelength patterns on a metallic surface. Specifically, a subwavelength-sized slit which is placed next to a periodic grating is designed and optimized to realize maximum coupling efficiency and directional radiation into a leaky-wave plasmonic mode. In this geometry, collective scatterings from the corrugations forming periodic gratings are synthesized to radiate towards the desired direction, and efficient beaming is achieved by properly manipulated the design parameters with a simple analytical model. Along with an effort to demonstrate the efficient directional beaming, we further prove that the directivity of beaming can be more enhanced by improving the slit-to-grating coupling efficiency. In demonstration of this concept, we employ the slit aperture which supports higher order

modal propagation inside in order to realize directional plasmon generation. The experimental results are the improved angular response of beaming in far-field radiation.

3.1 INTRODUCTION

Any form of waves spreads in all directions upon interacting with small object. Such wave behavior has been a classical problem in optics while being termed as diffraction phenomenon. It goes back the famous studies in 19th century by Tomas Young and Augustin-Jean Fresnel who triggered active discussions leading to the general acceptance of the wave theory of light diffraction, Although the general theory for spatially controlled objects has been widely acknowledged for various wave phenomena including diffraction and interference, recent discovery of extraordinary optical transmission [51-54] has re-drawn interest in tailoring the radiation from small apertures with surface waves. Within the recent progress in this field of research, the possibility of beaming the radiation from a small aperture using plasmons [55-59] has been reported as a potential way to realize directive optical radiation from subwavelength-sized sources.

By tailoring the collective scattering from small grooves, diffracted light can be out-coupled in desired direction. Springing from the demonstration of this beaming effect, various efforts have been made to realize and optimize directional beaming [57, 58] to pursue efficient optical energy transfer to free-space. Obviously, the realization of efficient light emission with high directionality is essential for several nanophotonic applications; however, directive optical radiation from aperture-based emitters is in general limited because of inherent diffraction from small apertures [56], which out-scatter light in all direction. In this chapter, we introduce and experimentally verify a method to realize efficient directional beaming from a slit-based light emitter coupled with surface-plasmon diffraction gratings. Our goal is to efficiently couple incident

energy into surface-plasmon modes and to tailor their propagation into directional leaky mode, while suppressing unwanted slit-related diffraction. We discuss how to design a slit-grating emitter with a special emphasis on the efficient light coupling between a slit and grating corrugations, through a simple analytical model derived from scattering wave equations. Efficient surface plasmon polariton (SPP) generation is then explored both theoretically and experimentally to enhance the radiation directivity.

3.2 ANALYTICAL MODEL FOR EFFICIENT DIRECTIONAL BEAMING

The geometry configuration under investigation consists of a subwavelength slit and an array of periodic gratings realized over a thick (spectrally opaque) silver film. In this configuration, the slit is primary used to couple transverse-magnetic (TM) light incident from transparent substrate (with an illumination angle of ϕ) on the back side of metal screen into surface plasmon modes launched at the metal/dielectric boundary.

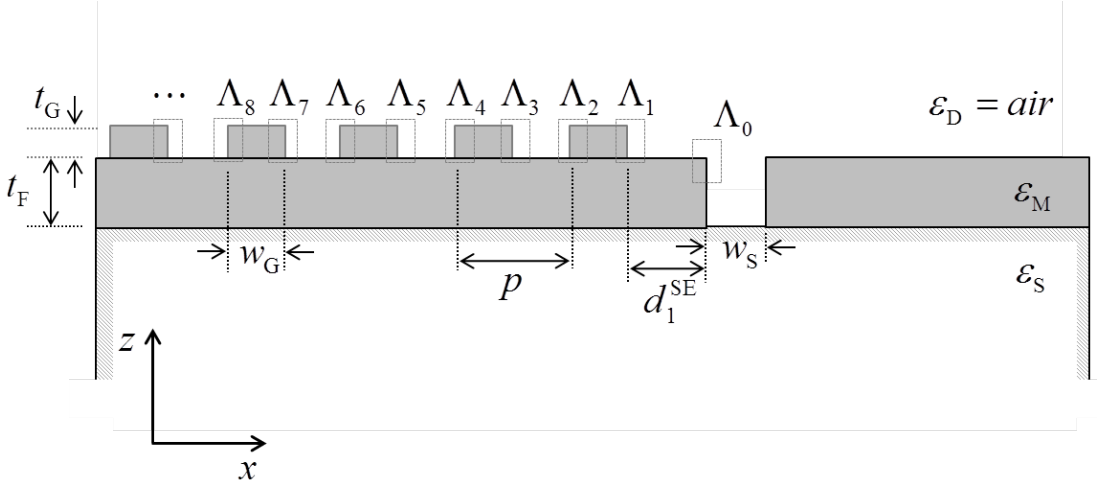

Figure 3-1: Sub-wavelength slit with a single-sided array of periodic corrugations. The geometrical parameters are: the grating pitch period p, thickness of metallic (ε_M) film t_F, grating thickness t_G, grating width w_G, slit width w_S, and the distance d_i^{SE} between Λ_0 and Λ_i. ϕ is illumination angle.

The coupled surface plasmon modes supported by the boundary will then diffract over the free space by periodic gratings. In this configuration, it is assumed that overall directional emission may be achieved with proper tailoring of the periodicity and morphology of gratings by perturbing the original surface plasmons into a directional leaky mode. The scattered wave from each individual corrugation is produced by the electromagnetic interaction of the surface plasmons supported by the metal interface and the obstacle, related through Helmholtz equation [54] . We first assume that the scattered wave $\mathbf{E_i^S}$ from each corrugation Λ_i can be written as a relation between the perturbed $\mathbf{E_i^P}$ and unperturbed fields $\mathbf{E_i^U}$ on the surface:

$$\begin{aligned}\mathbf{E}_i^S(x,z) &= \mathbf{E}_i^P(x,z) - \mathbf{E}_i^U(x,z) \\ &= A_i \iint k_o{}^2[\varepsilon_P(x',z') - \varepsilon_U(z')] \\ &\times \overline{\mathbf{G}}(x-x',z,z')\mathbf{E}_i^P(x',z')d\Lambda'_i,\end{aligned} \tag{3-1}$$

where $\overline{\mathbf{G}}$ is the Green's dyadic, and perturbed or unperturbed dielectric constants on the volume of the corrugation Λ_i are ε_P , ε_U . In the far-field and considering a perturbation method valid for small corrugations, the equation (3-1) can be simplified within an $\exp(j\omega t)$ time convention:

$$\begin{aligned}\mathbf{E}_i^S &\cong \iint k_o{}^2[\varepsilon_P(x',z') - \varepsilon_U(z')]\mathbf{E}_i^U(x',z')d\Lambda'_i \\ &\times \exp\left(-jk_o\rho + j\psi_0 - jk_{SP}d_i^{SE}\right),\end{aligned} \tag{3-2}$$

where $\rho = \left(x^2+z^2\right)^{1/2}$, $k_{SP} = 2\pi\left[\varepsilon_M\varepsilon_D/\left(\varepsilon_M+\varepsilon_D\right)\right]^{1/2}/\lambda$, and ψ_0 is the phase of scattering at the left slit edge Λ_0 .

One interesting finding in the Equation (3-2) is that the far-field scattering from the rising edge of the corrugation is out of phase with the one of the falling edge, if their distance from the SPP coupler is identical. We prove this conjecture by comparing the phase of scattered waves of simpler geometry. In Figure 3-2, we show that the scattered waves from the geometry consisting of a slit with a single type of edge (falling or rising edge). In this geometry, the scattering happens when the surface plasmons propagating along the metal/dielectric interface is perturbed by the edge. For this, we consider a subwavelength slit ($w_S = 50$ nm) perforated in the 250 nm thick Ag film with the edge located 1 μm away from its center, which is simpler form of periodic grating structure that will be further investigated.

By comparing the calculated scattered field and phase distribution, it is noticed that, especially for the normal direction to the plane of Ag film, the phase difference between scattered fields from falling and rising edge are out-phased to each other as predicted from the Equation (3-2). Although slight phase difference is observed due to the finite morphology of edge, in general phase property of scatterings generated by the edge follows the Equation (3-2).

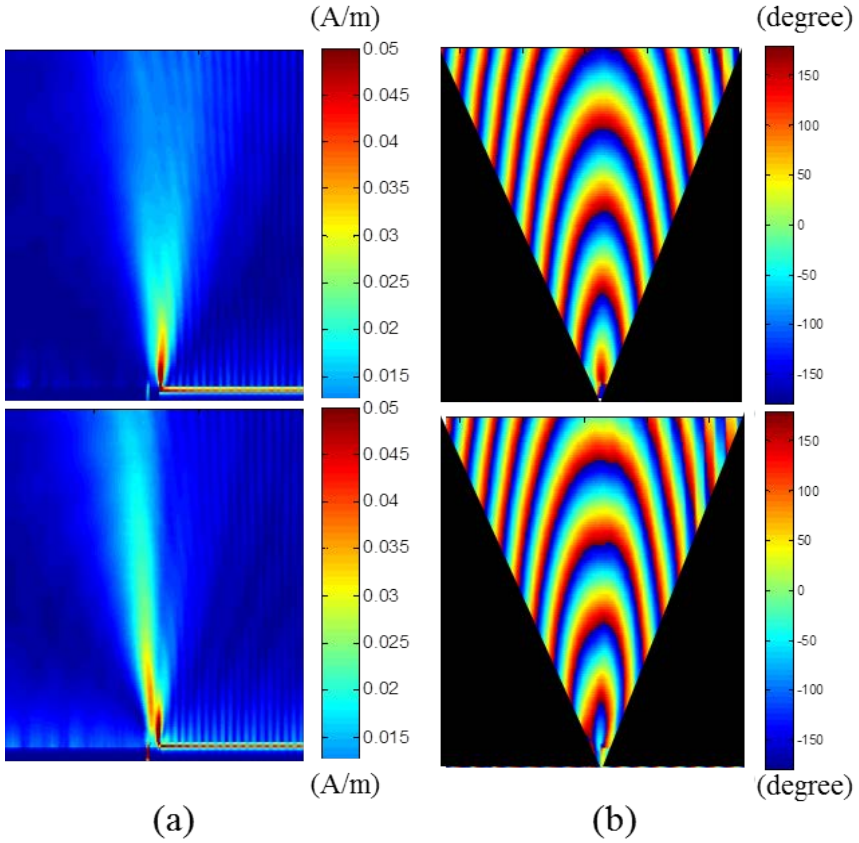

Figure 3-2 (a) Magnetic field $|H_y|$ and (b) phase distributions of scattered waves by rising (bottom row) and falling edge (top row). Each edge is excited by subwavelength slit (slit width $w_S = 50$ nm) which is located at $1\ \mu m$ away from its center.

For near the normal direction, radiation angle θ from $-20°$ to $+20°$, the phase difference between different scatterings are contained within from $-150°$ to $+150°$ as shown in Figure 3-3.

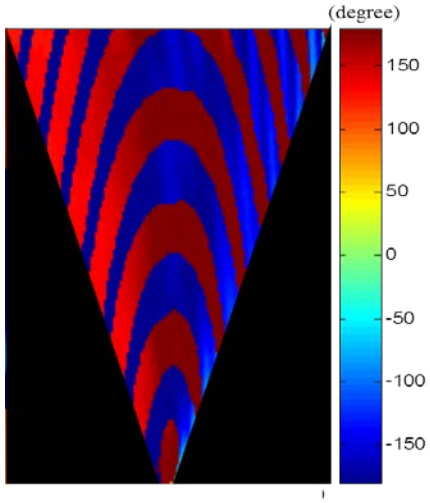

Figure 3-3 Phase difference of scattered waves from rising and falling edge.

This finding directly follows that a phase matching condition to construct a collimated directional beam, which can be obtained as:

$$k_{SP} d_i^{SE} = \begin{cases} d_i^{SE} k_o \sin\theta + m_i \cdot 2\pi & , i = \text{odd number} \\ d_i^{SE} k_o \sin\theta + m_i \cdot 2\pi - \pi & , i = \text{even number;} \end{cases} \quad (3\text{-}3)$$

where m_i is the diffraction order at the i^{th} edge. From the Equation (3-3), we can deduce key design parameters such as d_1^{SE} and the optimal ratio w_G / p to radiate in the desired direction, parameters that were otherwise obtained only with iterative numerical simulations [55, 57]. This analytical model can provide an initial approach for the optimal design parameters of the setup, which may be then optimized using full-wave numerical simulations.

3.3 EXPERIMENTAL DEMONSTRATION: DIRECTIONAL BEAMING

In order to apply these concepts in a practical scenario, a campaign of simulations and experimental investigations has been carried out. For numerical simulations, time-domain finite integration technique (FIT) of commercially available software, CST Microwave Studio™, was employed to characterize the proposed configuration in Figure 3-1 by varying several design parameters, starting from the design provided by Equation (3-2). After proper optimization, we have realized few optimal designs and experimentally measured the far-field radiation pattern in a setup consistent with the schematic model in Figure 3-4.

For sample preparation, 250 nm thick Ag ($\varepsilon_{\mathrm{M}} = -19 + j0.53$ at 630 nm [47]) film was evaporated (assisted by E-beam) on a BK7 ($\varepsilon_{\mathrm{S}} = 2.292$ at 630 nm) microscope slide and 60 nm thick Ag corrugations were patterned on the film by electron beam lithography, film deposition, and lift-off techniques. Finally, a sub-wavelength slit perforated in the Ag film was defined by focused ion beam (FIB) milling process. The fabricated slit-grating structure has a pitch period $p = 414$ nm and a ratio $w_{\mathrm{G}} / p = 0.5$ to realize maximum directional radiation at $\theta = 25°$ for the operating wavelength $\lambda = 630$ nm (FWHM of 10 nm for the supported leaky-mode). For the verification of Eqn. (3-3), interference patterns were measured in far-field and compared with simulations. For a given fixed grating configuration (fixed pitch period $p = 414$ nm and duty ratio $w_{\mathrm{G}} / p = 0.5$) but with different coupling distance d_1^{SE}, the expected radiation pattern is subject to a constructive or destructive interference following a periodic behavior with periodicity p, as a function of the coupling with the grating eigen-modes. To experimentally observe this effect, we realized a 200 nm width slit supporting only the fundamental waveguide mode, placed at controlled coupling distance from the grating structure (see insets in Figure 3-5(b)).

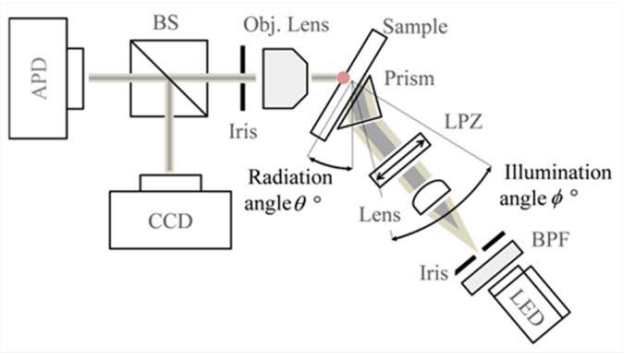

(a)

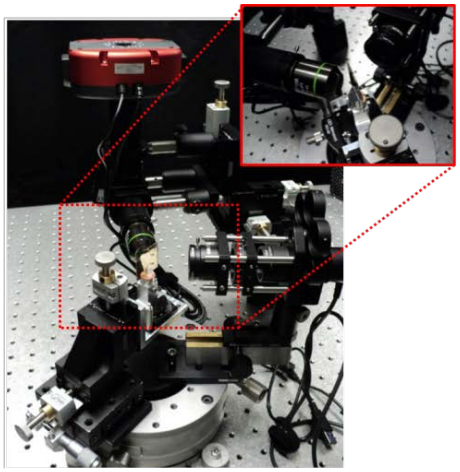

(b)

Figure 3-4: (a) Schematics of the optical setup, and (b) photographs of the setup, allowing for controlling both illumination angle ϕ and measurement angle θ.

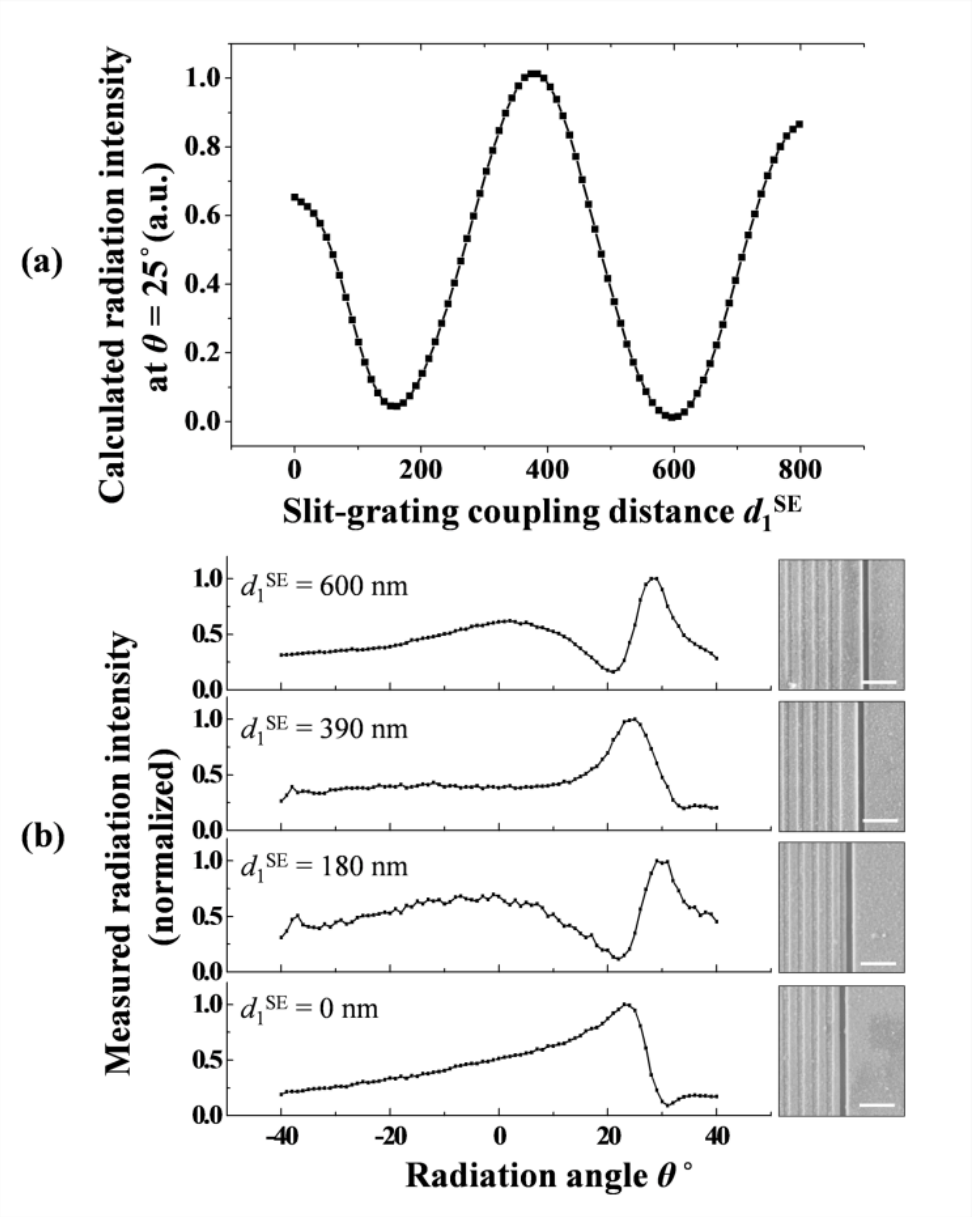

Figure 3-5: Radiation interference of slit-grating structure: (a) simulated radiation intensity at $\theta = 25°$ as a function of d_1^{SE} and (b) measured far-field radiation pattern for various values of d_1^{SE}. Each inset in (b) shows a scanning electron micrograph (SEM) image of structure corresponding to each d_1^{SE} value (scale bar: 1 μm).

Figure 3-5(a) shows the simulated intensity of directional radiation at $\theta = 25°$ varying d_1^{SE}, and Figure 3-5(b) presents the measured far-field radiation patterns for different d_1^{SE}. For the given grating geometry, as estimated by Equation (3-3), the intensity of directional beaming at a specific angle of interest is primarily governed by d_1^{SE}, showing a periodic behavior with periodicity p, due to constructive or destructive interference at about $\theta = 25°$. With such simple analytical tool, optical leaky radiation from a slit-grating structure as in Figure 3-1 may be modeled as the constructive interference of plasmonic grating diffraction and conventional slit diffraction, which would emit over a broad angular spectrum. In this respect, the key challenge to efficient directional beaming becomes the suppression of the slit diffraction and the maximum coupling of transmitted light through slit into a directive leaky mode supported by the plasmonic grating. Such challenges may be achieved through the combinational use of our slit-grating design approach and slit-based efficient SPP generation [60, 61]. Without changing the setup configuration, SPPs can be efficiently launched in a unidirectional manner by controlling the angle of tilted backside illumination and by employing the engineered width of the slit supporting its multimodal operation. Through slit-based efficient SPP generation, we achieve optimal conversion of the optical energy coupled through the slit into plasmonic modes and enhanced directional radiation. In addition, this approach allows suppressing conventional slit diffraction, increasing the overall directivity. Since the slit width and illumination angle are optimized to excite the plasmon mode at the slit exit aperture, we do not necessarily couple so easily with other radiation modes, producing an additional effective way of suppressing the conventional slit diffraction and direct the coupled energy primarily towards the grating leaky mode.

3.4 EXPERIMENTAL DEMONSTRATION: ENHANCED DIRECTIONAL BEAMING AIDED BY EFFICIENT SURFACE PLASMON GENERATION

Following this initial design, we explore the possibility of realizing more efficient SPP generation to achieve enhanced directional beaming. A geometry with $d_1^{\mathrm{SE}} = 0$ nm and $w_{\mathrm{S}} = 300$ nm was simulated and realized (see insets in Figure 3-5), with the idea of exciting higher-order guided modes inside the slit under oblique illumination [60]. The slit width of 300 nm was chosen to realize non-fundamental but mono-modal propagation with tilted illumination through the slab waveguide (i.e. perforated slit):

$$j\, w_{\mathrm{S}} \left(-\beta^2 + {k_0}^2\right)^{1/2} - m\pi = 2\tanh^{-1}\left[j\left(\beta^2 - \varepsilon_{\mathrm{M}} {k_0}^2\right)^{1/2} \Big/ \varepsilon_{\mathrm{M}} \left(-\beta^2 + {k_0}^2\right)^{1/2} \right] \quad (4)$$

where m is the order of modal slit propagation. The larger width supports more distinct modes that, with proper interference, can couple the energy in specific SPP directions for specific illumination angles. In our design $w_{\mathrm{S}} = 300$ nm was chosen to support two modes of guidance including the fundamental one. To evaluate the effectiveness of efficient SPP generation to produce directional beaming, numerical simulations have been carried out for the present geometry, analyzing the modal density profile with Fourier modal spectral analysis [62]. Figure 3-6 shows the calculated magnetic energy modal density $\left|H_y\left(k_x, z\right)\right|^2 = \left|\int H_y\left(x, z\right) e^{jk_x x} dx\right|^2$ profile above the structure for different angles of illumination, chosen following [60, 61] to couple the energy in different directions of SPP propagation: SPP generation towards the side without grating (Figure 3.6(a)), towards both sides (Figure 3.6(b)), and towards the side with corrugations (Fig. 3.6(c)) were obtained for different optimal values of ϕ. Each inset shows the total angular power spectrum within the region of simulation. For the case in which SPPs are efficiently generated on the grating side, more optical energy is concentrated around k_{DIR}, corresponding to radiation at about $\theta = 25°$; in comparison to Figure 3-6(a) and

(b), the case in Figure 3-6(c) shows increased energy coupling efficiency into leaky radiation within radiation angles between 20° to 30° by 160 % and 65 %, respectively.

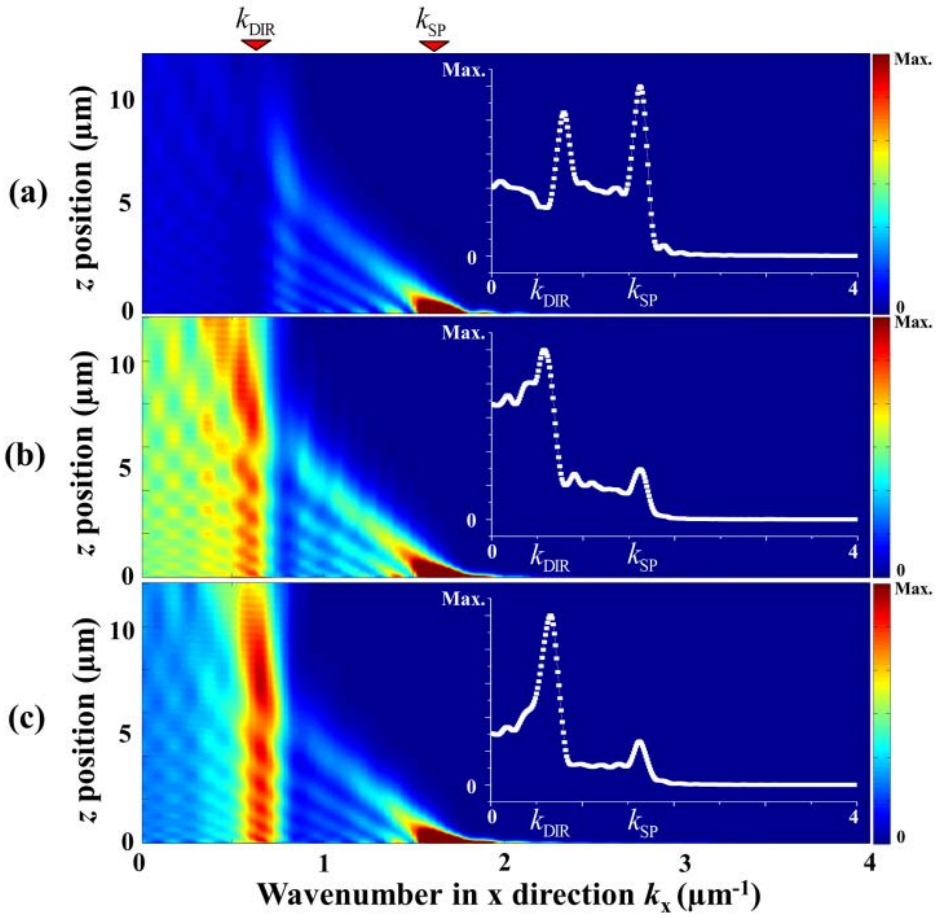

Figure 3-6: Calculated magnetic energy modal density $\left|H_y(k_x, z)\right|^2$ above the slit-grating structure and total power spectrum (each inset) for enhanced SPP generation toward the (a) non-grating side $(\phi = -32.6°)$, (b) both side $(\phi = 0°)$ and (c) grating side $(\phi = 32.6°)$. The optimal impinging angle ϕ for efficient SPP generation has been calculated as shown in Ref. [60, 61].

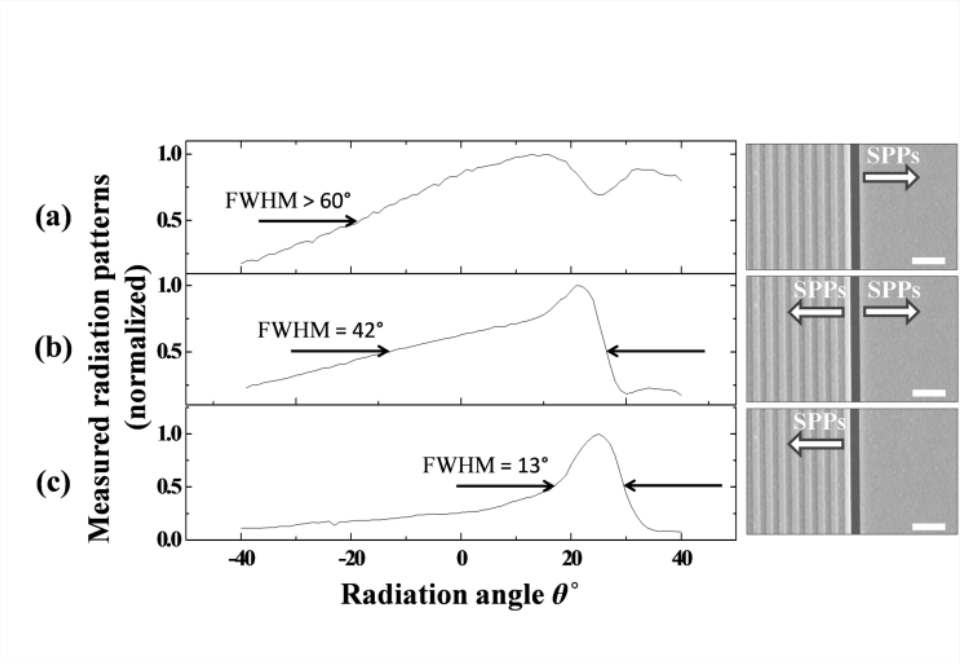

Figure 3-7: Measured radiation patterns of the proposed structure with $d_1^{SE} = 0$ nm $w_S = 300$ nm for the case of SPP generation toward (a) non-grating side, (b) both sides, and (c) grating side. Note that measured results, (a), (b), and (c), correspond to the simulations in Figure 3.6(a), (b), and (c), respectively. Each inset shows a SEM image of structure with a direction indicator of launched SPPs (scale bar: 1 μm).

Evidence of enhanced directional beaming can be further obtained by observing the full-width-at-half-maximum (FWHM) angle of radiation. Since more energy is confined in the spectral range of directional radiation k_{DIR}, one can expect sharper angular response in the far-field radiation pattern. Experimental measurements of such enhanced directional radiation are shown in Figure 3-7 (c) (corresponding to the simulation in Figure 3-7(c)), to be compared with Figure 3-7(a) and (b) (corresponding to simulations in Figure 3-6(a) and (b), respectively). In Figure 3.7(c), as expected, the measured directional beaming is enhanced via efficient SPP generation on the grating side, so that

the obtained FWHM is drastically reduced in comparison to the case in which SPPs are launched on both sides. In contrast, no significant directional beaming is obtained if the SPPs are generated on the side without grating (see Figure 3-7(a)), as expected.

3.5 CONCLUSION

In this chapter, we have discussed analytical models, numerical simulations and experimental results to control the plasmonic diffraction from a sub-wavelength slit coupled to an array of periodic corrugations. We offer the analytical solution to find key design parameters for the realization of efficient directional beaming, and they have been optimized for the experimental demonstration. With the initial design, we prove the efficient directional beaming mechanism. Further enhancement of directionality was also achieved through efficient SPP generation and coupling to the grating, by selecting the slit design and the illumination angle. Our far-field measurements agree well with the presented analytical and numerical results.

Chapter 4: Tunable Directional Radiation

4.1 INTRODUCTION

Tailoring the electromagnetic radiation of an array of antennas is a classic subject of interest in many research areas since its first explorations in 1905 by Karl Ferdinand Braun. At microwaves and radio frequencies, phased arrays are commonly used to scan a directive radiation pattern in the angular spectrum. By manipulating the relative phase of the signal feeding each antenna element, radiation can be pointed towards the desired direction and suppressed in all others [63, 64].

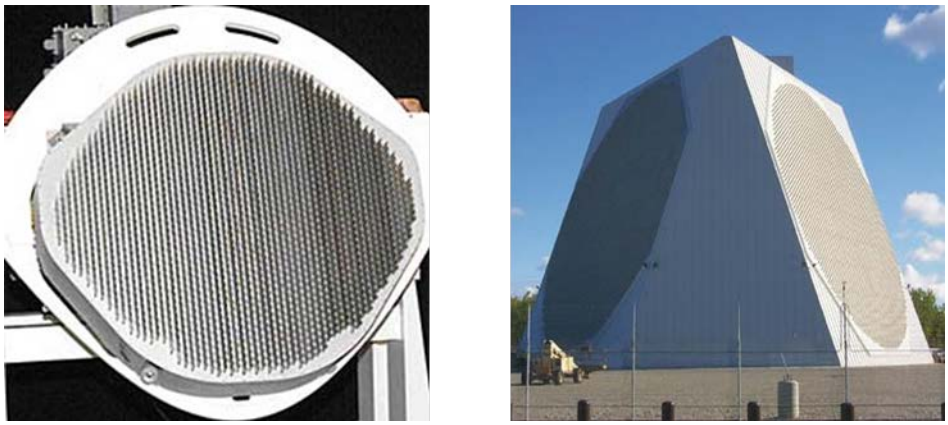

Figure 4-1: Example of phased array antennas. AN/APG-77 F-22 Radar [64] (left) and PAVE PAWS Radar at Clear AFS, Alaska [63] (right).

One useful feature provided by phased arrays is dynamic beam sweeping: by actively modifying the phase with which each element is driven, it is possible to tailor the overall radiation towards an arbitrary direction and suppress undesired radiation in other directions. A similar approach may be applied in plasmonic nano-optics, where an array of small scatterers [65-73] may be used to realize directive optical radiation. By modifying the phase of the excitation of each radiator, the collective optical radiation may be directed and dynamically manipulated towards the direction of interest. Recently,

Yagi-Uda nanoantennas [65-69, 72] consisting of parasitically phased elements driven by a confined quantum source have been demonstrated at optical frequencies, providing directional emission from the nanoscale to the far-field. Similarly, slit-based patterned planar surfaces have been reported showing directive optical radiation [53, 55-60, 74]. Albeit various design efforts have been spent to develop directive and controlled radiation for relevant applications in nano-optics, limited experimental efforts showing the possibility of dynamic beam sweeping have been reported [59].

4.2 METHODOLOGY

In this section, we focus on a nanopatterned metallic surface over which tunable directional optical radiation is realized using a subwavelength slit coupled on one side to an array of periodic gratings. The directive radiation is based on the leaky-wave mode supported by the periodic structure in a given frequency band of interest. In the proposed configuration, the subwavelength slit excites the array over a plasmonic screen, launching surface plasmon polaritons (SPPs) that are converted into leaky modes by the proper periodic corrugations. The coupling between the excitation and the SPP mode is maximized by controlling the slit width through nanofabrication and the angle of excitation, so that SPPs are generated primarily on the grating side [48, 60, 61] to maximize the coupling efficiency with the leaky-wave mode [48]. This solution has also the advantage of suppressing the conventional slit diffraction and unwanted side lobes for a specifically optimized oblique angle of illumination. Similar to radio-frequency leaky-wave antennas [75, 76], it is then possible to sweep the direction of optical radiation by manipulating the effective electrical distance between the scatterers.

The proposed optical phased array consists of an array of periodic metal bumps driven by a slit aperture, which couples incident transverse-magnetic (TM) light into

plasmonic modes. In this configuration, shown in Figure 4-2, a one-dimensional (1D) array of periodic metal bumps serves as a directive optical antenna, effectively converting the dominant SPP mode into a leaky-wave mode radiating in free space. Previously we have studied efficient directive radiation from metal bumps excited by SPPs [48].

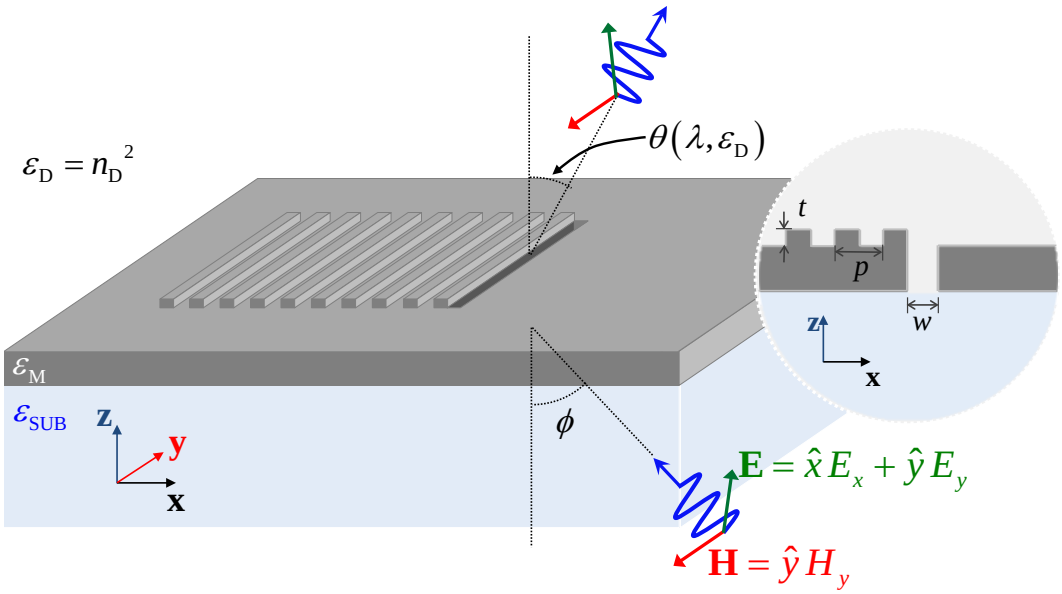

Figure 4-2: Schematic of a tunable directional optical antenna: a subwavelength slit with a left-side array of periodic gratings, consisting of corrugations in a plasmonic screen. Note that ε_D, ε_M, and ε_{SUB} indicate the relative permittivity of surrounding medium, metal, and supporting substrate (BK7), respectively. Directive radiation at a specific angle θ can be achieved by a proper choice of surrounding medium ε_D and wavelength of operation λ; and its directivity can be further enhanced by optimizing illumination angle ϕ.

In our model, we have shown that the phase matching condition to form a collimated directive leaky-mode within the first diffraction order of each scatterer is given by

$$p\left(\mathrm{Re}\left[k_{SP}\right] + k_D \sin\theta\right) = 2\pi\,, \qquad (4\text{-}1)$$

where, the SPP wavenumber is $k_{SP} = 2\pi\left[\left(\varepsilon_M \varepsilon_D\right)/\left(\varepsilon_M + \varepsilon_D\right)\right]^{1/2}/\lambda$, which is perturbed into a directive leaky-wave mode with wavenumber $k_D = 2\pi\sqrt{\varepsilon_D}/\lambda$ by the periodic corrugations, ε_D is the dielectric permittivity of background, ε_M is the metal permittivity, θ is the angle of radiation, and p is the array periodicity. We assume that the permittivity of all involved materials is dispersive hence a function of the operating wavelength λ. Since the effective electrical length $p \cdot \mathrm{Re}\left[k_{SP}\right]$ and $p \cdot k_D \sin\theta$, governing the matching condition in Equation (4-1), are controllable by the operating wavelength and background permittivity, we may tune the direction of optical radiation by tuning either one of these quantities. Following the design methodology [18], we choose initial design parameters to realize maximum radiation at $\theta = 25°$ for operating wavelength $\lambda = 630$ nm and free space ($\varepsilon_D = 1$). It is important to note that the proposed configuration can tailor light into any propagating mode of interest. Even though we focus on coupling energy to free-space with leaky modes, light may also be coupled to surface plasmon modes by properly choosing the design parameters [48].

For the excitation of such optical phased array consisting of periodic metal bumps, a perforated slit in plasmonic screen is chosen to serve as a driving element, providing efficient conversion of incident TM light into surface plasmon modes [48, 60, 61]. With tilted illumination, a perforated slit that supports higher-order guided modes can provide unidirectional generation of SPP at its exit, maximizing the radiation efficiency of this system. The mode supported by a plasmonic slit follows the dispersion equation:

$$i\left[w\left(-\beta^2 + {k_D}^2\right)^{1/2} - m\pi\right] = 2\tanh^{-1}\left[i\varepsilon_D\left(\beta^2 - \varepsilon_M {k_D}^2\right)^{1/2}/\varepsilon_M\left(-\beta^2 + {k_D}^2\right)^{1/2}\right]. \quad (4.2)$$

A slit width $w = 300$ nm is therefore chosen to support the higher-order ($m = 1$) guided mode, which may couple energy into the desired SPP only on the side of the grating for a specific excitation angle.

We adopted nanofabrication technologies capable of producing sub-100 nm feature size to realize such optical phased array as in Figure 4-2. First, 250 nm thick Ag film was deposited on BK7 slide with 3 nm thick Ge layer serving as a wetting layer [77] to enhance adhesion and surface quality of the Ag film. Opposite to the case presented in Ref [78], the thickness of the Ag film was chosen to be thick enough so that SPPs at the metal/BK7 interface would not to leak through the film for the case the of surrounding index n_D is higher than that of BK7. An array of Ag bumps on the surface, with periodicity $p = 414$ nm and duty ratio 0.5, was formed on the Ag film to provide a 1st order plasmonic grating diffraction. General E-beam lithography (JEOL 6000 FSE, JEOL Ltd, Tokyo, Japan) and lift-off techniques were used with a bi-layer PMMA process (495K C4/950K C4, MicroChem Inc., MA, USA) to construct a $t = 60$ nm height array of gratings. A slit was then defined and perforated in Ag film right next to the array by focused ion beam (FEI SEM/FIB dual beam, FEI Corp., OR, USA) milling. The milled slit had a width of 300 nm to support a higher-order mode of slit transmission, necessary for high coupling efficiency [48, 60, 61] and improved directive radiation [48], as discussed in the previous section. The distance between the left-most slit edge and the first rising edge of the corrugations was kept to 0 nm, following our theoretical investigations [48]. Finally, on top of the fabricated plasmonic configuration (consistent with Figure 4-2), flat BK7 coverslip (~200 μm in thickness) was added with 80 μm thick PDMS spacer to create a space to introduce various index matching fluids (Cargille-Sacher Laboratories Inc., NJ, USA).

4.3 EXPERIMENTAL RESULTS AND

The radiation patterns from the fabricated device were then characterized with a custom optical setup allowing us to control the angle of both illumination and radiation. The angular intensity profile was recorded on a CCD, as shown in Figure 4-3. A 300 nm slit was excited with oblique backside illumination of a collimated TM plane-wave at a specific wavelength of operation. A broadband white light emitting diode (LED) was used with a bandpass filter to acquire the desired spectra at the output. Angular-dependent optical signals from the device were collected with low numerical aperture (NA) optics (Olympus LMPlan X20/0.4 with closed iris) and captured by a charge-coupled device (CCD). The fabricated device and illumination optics were mounted on separate three-axis alignment systems with rotational stage, allowing for the control of both illumination and measurement angles. Detailed intensity profiling for angular dependent radiation are provided in Figure 4-3.

We experimentally demonstrate a tuning mechanism for directional radiation and beam sweeping in this setup (see Figure 4-2 and Figure 4-3), obtained by changing the background medium around the corrugations. As typical in leaky-wave antenna setups [75, 76], we are also able to track the single-beam sweeping associated with varying the wavelength of operation. Along with the characterization of tunable directive radiation, we also discuss and verify that efficient SPP coupling can be an effective tool to improve the directionality under index-mediated tuning mechanisms. Our experimental setup does not allow to directly evaluate the SPP coupling efficiency [49, 79, 80] through a slit to extract the overall radiation efficiency of the proposed configuration, but we use modal spectral analysis for this purpose. By measuring the full-width-at-half-maximum (FWHM) angle of radiation, the proposed configuration can be qualitatively characterized. Since the diffraction grating supports directive radiation at a specific angle,

efficient generation of SPPs toward gratings and conversion into directive leaky mode will result in sharper angular response [48]. Measured radiation patterns for the two tuning mechanisms are presented in Figure 4-4.

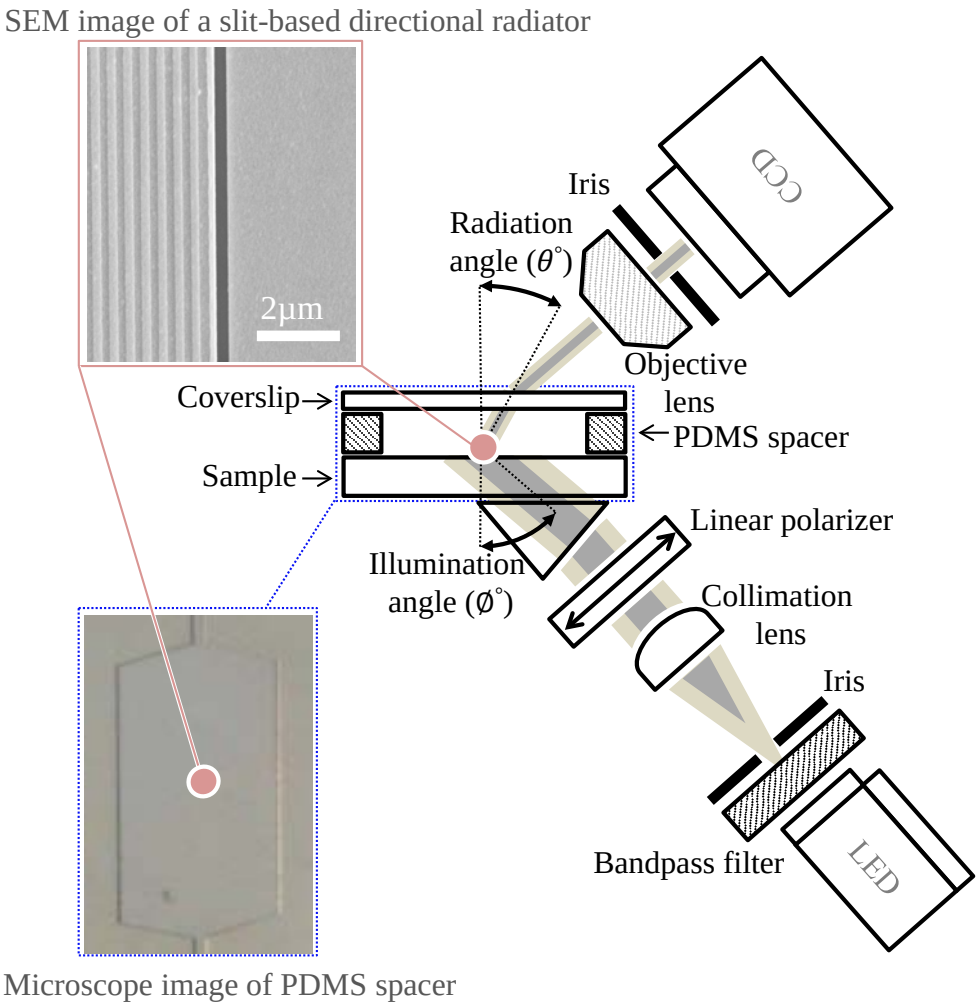

Figure 4-3: Radiation pattern profiles from CCD images captured at various angles for $\lambda = 630$ nm and no index matching fluid in the spacer.

In Figure 4-4(a), radiation patterns were recorded after varying the index range of matching fluids $n_D = \varepsilon_D^{1/2} = 1.26 \sim 1.62$ at the fixed wavelength $\lambda = 630$ nm. We note

that the weak frequency dispersion of each index matching fluid is not significant within the spectral bandwidth considered in each measurement, as it is contained within an index variation of less than 0.001. In illuminating the slit, we used TM polarized light at the operating wavelength with 10 nm of spectral FWHM bandwidth. In Figure 4-4(b), conversely, we show beam scanning changing the wavelength of illumination ($\lambda = 500 \sim 650$ nm), in the absence of index matching fluids ($n_D = 1$). Also here, the spectral FWHM for each illumination was 10 nm. To compare the angular shift and the angular confinement of radiation pattern (angular FWHM) for both tuning mechanisms, each recorded pattern in Figure 4-4 is normalized with respect to its peak radiation intensity.

As seen in Figure 4-4, we have experimentally demonstrated the two tuning mechanisms scanning directive radiation. By varying the background refractive index ($n_D = 1.00 \sim 1.62$), we achieve a shift of peak radiation angle of about 39.7°; and by varying the wavelength of operation from 500 nm to 650 nm, the peak radiation angle θ changes from -1° to +27°. Detailed angular sensitivity of directive radiation with respect to these tuning mechanisms is summarized in Figure 4-5. As expected, nearly linear variation with the angle of radiation is found, both in terms of wavelength of operation and of change in the refractive index. The angle may scan from positive values to broadside radiation, with interesting implications for beam scanning, optical communications and plasmonic sensors at the molecular scale.

(a)

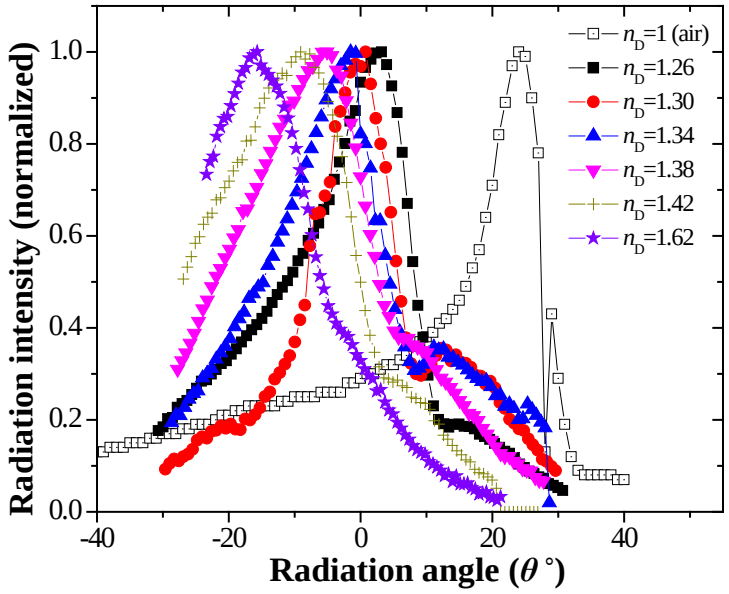

(b)

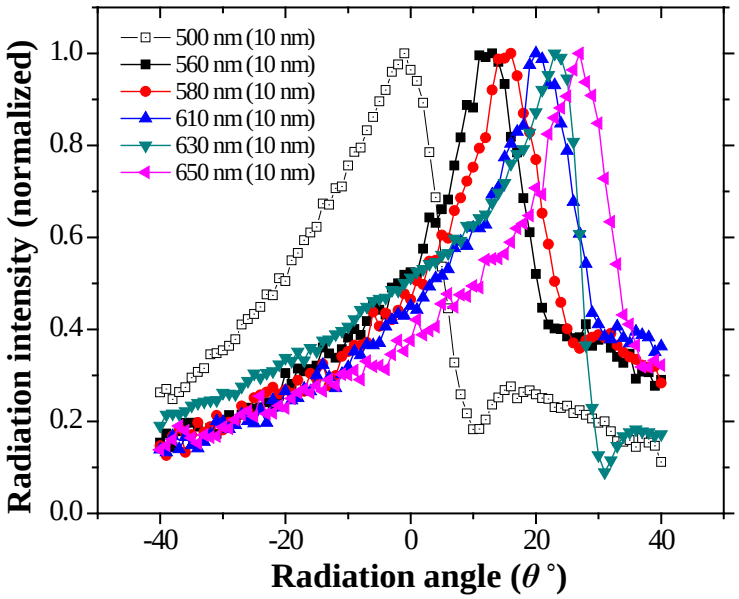

Figure 4-4: Measured far-field radiation patterns from the proposed configuration with (a) various index matching fluids and (b) various wavelengths of operation. TM polarized light with spectral FWHM of 10 nm was used throughout experiments. Note that each recorded radiation pattern is normalized to its peak intensity.

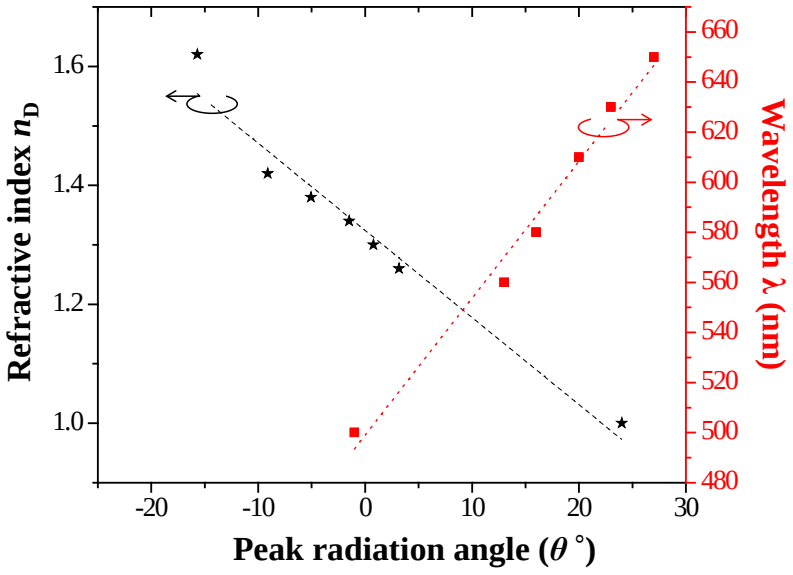

Figure 4-5: Peak radiation angle as a function of wavelength (black) and the refractive index of surrounding medium (red). Each dashed line is a fitting curve for varying peak radiation angle.

4.4 CONCLUSIONS

Throughout the experiments, the illumination angle ϕ was carefully selected at each wavelength and each index matching fluid to maximize the coupling efficiency with the SPP toward the grating side, according to the theory presented in [48, 60, 61]. Since the modal propagation inside the slit is a function of both wavelength and the refractive index of the fluid, as well as the geometric parameters, different values of illumination angles had to be selected in each experiment. The evidence of improved directive optical radiation with an idea of tilted illumination of slit can be found in Figure 4-6 for one of the experimental results, for an index matching fluid $n_D = 1.34$ and wavelength $\lambda = 630$ nm. By exciting the slit at normal incidence and at the optimized ncidence angle of 26°, we find a drastic difference in overall radiation directivity, achieved by suppressing the unwanted side lobe and reducing the angular FWHM of the radiation

pattern from 36.0° to 19.1°. As expected, the radiation peak is mostly the same for the two excitations, since the leaky-mode supported by the grating is not affected by the SPP excitation mechanism. These results are consistent with our previous studies on efficient directional beaming [48]. Similar to the case of SPPs guided toward diffraction gratings, herein the overall directivity can be drastically improved by optimizing the slit width and the angle of illumination to properly couple SPPs to the grating and eliminate undesired diffraction effects from the slit.

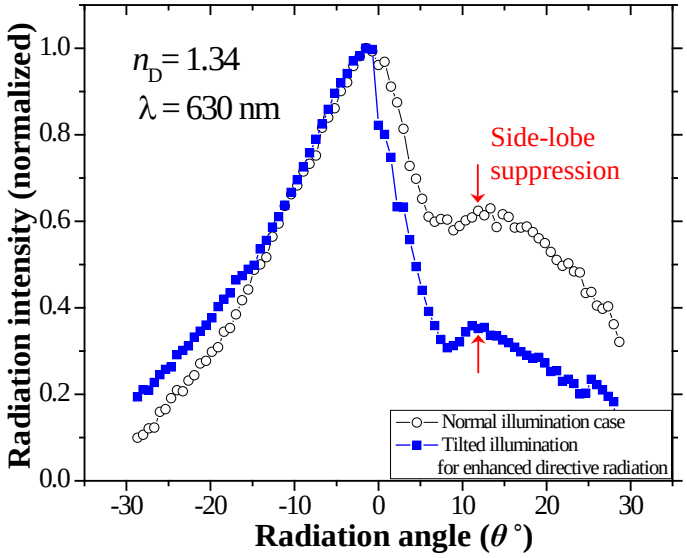

Figure 4-6: Measured radiation patterns of the configuration shown in Fig. 1 for normal illumination (black curve, open circle) and tilted illumination (blue curve, filled box) for enhanced directive radiation. Index matching fluid with a refractive index of 1.34 was introduced and TM polarized light at 630 nm was used to excite the slit. Measured FWHM for normal incidence was 36.0°; whereas the case for tilted illumination was 19.1°.

As discussed above, it is important to note that the proposed geometry offers comparable sensitivity to conventional SPR based devices. For instance, the proposed configuration shows an angular sensitivity satisfying the relation $\delta\theta_{DR} \approx -\delta\varepsilon \cdot \lambda_0 / 2p$ upon the

presence of small dielectric perturbations in the surrounding medium ($\varepsilon_D = 1 + \delta\varepsilon$) if $\left|\mathrm{Re}(\varepsilon_M)\right| >> 1$ and $\left|\delta\varepsilon\right| << 1$ are assumed. Such sensitivity is comparable to that of conventional Kretschmann configuration [81], so we may find potential sensing applications based on dielectric perturbations.

In summary, we have experimentally demonstrated that the emission from a slit in a plasmonic screen may be directed in a specific direction of choice by coupling it with a compact grating system patterned on one side of the slit in the plasmonic surface. The radiation can be tuned to a large degree by varying the wavelength of operation and/or the index matching fluid surrounding the grating. Potential applications of this effect may be envisioned in tunable nano-optical devices and optical wireless links tunable in real-time. In addition, the sensitivity to such tuning mechanisms may be utilized for chemical and biomedical applications for which the spectral signature of samples could be identified.

II. SPECTRAL MANIPULATION OF LIGHT

In this part, we present our study on the spectral manipulation of light using periodic slit-grating structure. Specifically in the Chapter 5, we investigate the theoretical mechanism of bandgap on plasmonic network geometry consisting of slit-grating with embedded horizontal waveguide. We theoretically prove that modal resonance coupled from radiation can form an omnidirectional bandgap invariant to the angle of incidence. First, the slit-grating geometry having a horizontal waveguides across on E-plane is considered and its bandgap mechanism is analyzed by transmission-line approach. Extended from bandgap mechanism, we also propose the mechanism of proposed geometry in which efficient transmission occurs. Based on the transmission-line approach again, we prove that such efficient transmission is associated with impedance matching condition where the reactance imposed by slit-gratings is compensated by horizontal waveguide. Using the proposed transmission mechanism, we experimentally show that the condition for efficient light transmission can be tailored by modifying the local/bulk index around the geometry. Details of such tunable transmission are presented in Chapter 6.

Chapter 5: Sharp Omnidirectional Bandgap and Non-resonant Transmission

In this chapter, we discuss the creation of an omnidirectional photonic bandgap in a grating formed by a pair of plasmonic patterned thin screens, governed by coupled resonant modes. Around the resonance, the grating reflects the impinging wave independent of the incidence angle, while remaining essentially transparent at lower frequencies. Modeling the geometry as a two-dimensional metal-dielectric-metal plasmonic waveguide loaded by stubs, we prove that this phenomenon is based on

coupled resonant modes, mimicking a thin resonant impedance sheet. Our transmission-line model predicts two distinct resonant bandgaps, omnidirectional and quasi-omnidirectional in nature, and provides design tools to tailor their optical properties in the frequency spectrum. Another finding that we prove in this chapter is that the transmission spectrum peak near the sharp omnidirectional bandgap may not count on the resonant transmission. Based on the transmission-line model, we show that the peak transmission is rather related to the reactive impedance of slits and the efficient transmission happens when the those reactance is compensated by stub impedance.

5.1 INTRODUCTION

The resonant response of diffraction gratings is usually associated with sharp field variations over a narrow frequency or angular band. Since the first observation [19] and confirmation [22, 26] by Wood and Rayleigh, these phenomena have been widely studied by many researchers, including Fano [20] who offered a breakthrough in the theoretical understanding of these resonant anomalies. The widely accepted mechanism on which they are based, as pointed out by several seminal papers [20, 21], consists in the complex field interaction of guided modes supported by periodic gratings. The accurate prediction of the dispersion of these modes has been greatly simplified with the advent of rigorous vector models, and the concept of coupled resonances [82, 83] has become a topic of interest, envisioning new applications of optical gratings. Recent studies [84-91] have shown the potential of local oscillators arrays coupled with the impinging light, and some of them have reported significant suppressed transmission [84-86, 90, 91] at resonance, despite their thin features. Although the resonant bandgap response usually appears weak, especially for sparse array configurations [85, 91], significant resonant anomalies may be achieved with proper designs, that allow a strong coupling of the impinging light with

modal resonances. In order to realize such condition, we consider a geometry whose electromagnetic interaction is described by well-defined waveguide modes, such as an open-ended waveguide phased array, inspired by similar geometries at lower frequencies.

5.2 BANDGAP MECHANISM

In this section, we introduce the resonant photonic bandgap mechanism of a two-dimensional (2D) grating based on a metal-dielectric-metal (MDM) plasmonic waveguide network. By realizing coupled resonance modes in this easily modeled geometry, we show that an effective control of resonant suppression of transmitted light can be achieved. Depending on the resonance mode and its resulting standing wave, the presented mechanism is weakly dependent on the incidence angle but highly selective to the frequency of operation, which open interesting possibilities in sharp filtering and sensing with high resolution. Our finding represents an extended study on resonant optical anomalies in engineered metal corrugations, proving that their anomalies can be manipulated through the modulation of guided waves. In details, two distinct bandgaps are predicted by our model in the proposed geometry, an omnidirectional bandgap and a quasi-omnidirectional bandgap, as described in the following.

Consider a freestanding MDM film perforated with one-dimensional (1D) periodic gratings of periodicity p and slit width w_S, illuminated by a transverse-magnetic (TM) mode (see Figure 6-1). In this configuration, we assume that the slit width w_S and dielectric thickness w_D are small compared to the wavelength of operation λ, and that the metal thickness t_M is significantly thicker than the skin depth at the frequency of operation, conditions that ensure the propagation of only one fundamental mode in the MDM waveguide formed by the two perforated metal screens. To analyze the scattering from this structure, we employ a transmission-line (TL) approach, based on

the effective characteristic impedance [51, 52] that takes into account of the scattering from guided modes in the MDM waveguide. Based on its modal dispersion, the structure in Figure 5-1 can be modeled as an MDM waveguide loaded by series stubs, representing the slits. Its equivalent TL network model forms "a series junction", as depicted in Figure 5-1, consistent with conventional "E-plane waveguide junctions" [92] loading a parallel-plate waveguide.

Due to its periodic nature, the proposed geometry can be modeled as a TL network consisting of a ladder of TL unit-cells each excited with a different phase $\phi = p \cdot k_0 \sin\theta$ for a given incidence angle θ. The surrounding free space is then modeled in each unit cell as a semi-infinite TL, with wavenumber $\beta_0 = k_0 \cos\theta$ and characteristic impedance per unit length $Z_0 = p\left(\mu_0/\varepsilon_0\right)^{1/2}\cos\theta$. The modal propagation in a simple *plasmonic* MDM waveguide satisfies the dispersion relation [93] $w_{\mathrm{D|S}}\sqrt{\beta_{\mathrm{D|S}}^2 - k_0{}^2} = 2\tanh^{-1}\left[\left(-\sqrt{\beta_{\mathrm{D|S}}^2 - \varepsilon_{\mathrm{M}}k_0{}^2}\right)\Big/\left(\varepsilon_{\mathrm{M}}\sqrt{\beta_{\mathrm{D|S}}^2 - k_0{}^2}\right)\right]$, where ε_{M} is the metal relative permittivity; and β_{D} and β_{S} are the modal wavenumber in the MDM waveguide and in the slit, respectively. Since we consider the fundamental TM mode, its characteristic impedance per unit length is written as

$$Z_{\mathrm{D|S}} = \frac{V}{I} = \frac{\int_0^{w_{\mathrm{D|S}}} \beta_{\mathrm{D|S}}\mathrm{H}/\left(\omega\varepsilon_0\right)}{\mathrm{H}} \cong \frac{w_{\mathrm{D|S}}\beta_{\mathrm{D|S}}}{\omega\varepsilon_0}. \qquad (5\text{-}1)$$

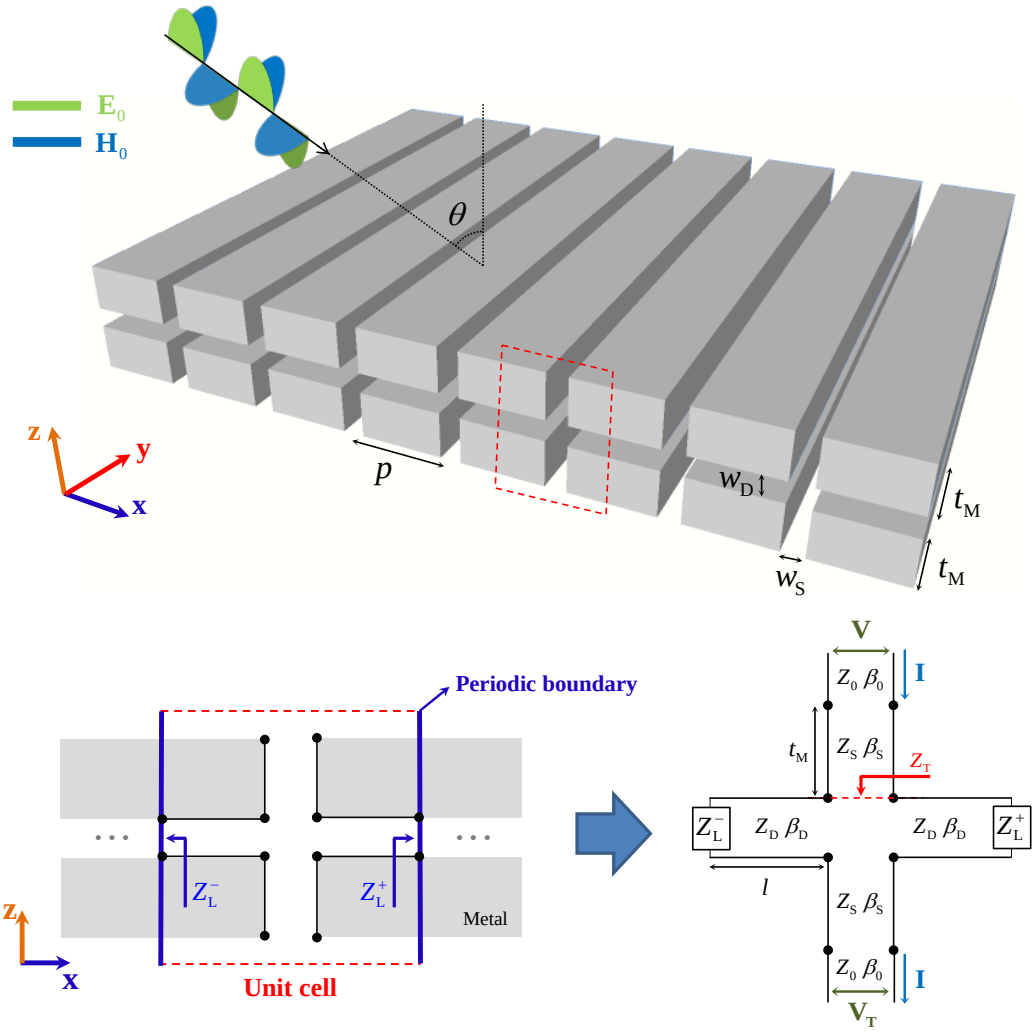

Figure 5-1: The proposed geometry: a 2D plasmonic grating forming a loaded waveguide (top) consisting of a series of unit cells (bottom left) with equivalent circuit model shown in the bottom right panel. p is the period, $l=(p-w_D)/2$ is the stub length, w_D and w_S are the widths of dielectric layer and slit, t_M is the metal thickness, and θ is the incident angle. The equivalent load impedance $Z_L^{\pm}$ is readily found by comparing the magnetic-field ratio for forward and backward waves at the periodic boundary.

By employing the concept of equivalent load impedance $Z_{\mathrm{L}}^{\pm}$, representing the scattering at the boundaries, the proposed TL network may be further simplified to the equivalent TL circuit in Figure 5-1(bottom right) with asymmetrically-loaded series stubs. The equivalent load impedance can be readily evaluated by comparing the magnetic-field ratio for forward and backward Bloch components $\gamma_{\mathrm{H}}^{\pm}$ at the unit cell boundaries (+ for right and – for left periodic boundary), following the relation $Z_{\mathrm{L}}^{\pm} = Z_{\mathrm{D}}\left(1\text{-}\gamma_{\mathrm{H}}^{\pm}\right)\Big/\left(1+\gamma_{\mathrm{H}}^{\pm}\right)$. In deriving $\gamma_{\mathrm{H}}^{\pm}$, the concept of transfer function matrices is used to take into account the multiple scattering from the infinite number of unit cells, exploiting the periodicity of the geometry and of the excitation, leading to the simple relation:

$$\gamma_{\mathrm{H}}^{\pm} = \sin\left(\mp\phi/2 + \beta_{\mathrm{D}} l\right)\Big/\sin\left(\pm\phi/2 + \beta_{\mathrm{D}} l\right). \tag{5-2}$$

Subsequently, the reflection coefficient at the entrance of the slits may be written as

$$r_{\mathrm{H}} = \frac{iZ_{\mathrm{S}}\left(Z_{\mathrm{T}} - Z_0\right) + \left(Z_{\mathrm{S}}^2 - Z_{\mathrm{T}}Z_0\right)\tan\left(\beta_{\mathrm{S}} t_{\mathrm{M}}\right)}{iZ_{\mathrm{S}}\left(Z_{\mathrm{T}} + Z_0\right) + \left(Z_{\mathrm{S}}^2 + Z_{\mathrm{T}}Z_0\right)\tan\left(\beta_{\mathrm{S}} t_{\mathrm{M}}\right)}, \tag{5-3}$$

where the input impedances per unit length at the series junctions are:

$$Z_{\mathrm{T}} = Z_{\mathrm{D}}\frac{Z_{\mathrm{L}}^{+} - iZ_{\mathrm{D}}\tan\left(\beta_{\mathrm{D}} l\right)}{Z_{\mathrm{D}} - iZ_{\mathrm{L}}^{+}\tan\left(\beta_{\mathrm{D}} l\right)} + Z_{\mathrm{D}}\frac{Z_{\mathrm{L}}^{-} - iZ_{\mathrm{D}}\tan\left(\beta_{\mathrm{D}} l\right)}{Z_{\mathrm{D}} - iZ_{\mathrm{L}}^{-}\tan\left(\beta_{\mathrm{D}} l\right)} + Z_{\mathrm{S}}\frac{Z_0 - iZ_{\mathrm{S}}\tan\left(\beta_{\mathrm{S}} t_{\mathrm{M}}\right)}{Z_{\mathrm{S}} - iZ_0\tan\left(\beta_{\mathrm{S}} t_{\mathrm{M}}\right)}.$$

(5-4)

In the lossless limit, the magnetic-field ratio $\gamma_{\mathrm{H}}^{\pm}$ is a real-valued function of the incident angle θ, associated with the imparted phase ϕ; its value becomes unity ($\gamma_{\mathrm{H}}^{\pm} = 1$) regardless of the variation of θ under the coupled resonance condition

$\beta_D l = \pi(m+1/2)$ (with m being an integer) along the transverse direction. This condition directly corresponds to the formation of a symmetric resonance in the MDM waveguide with respect to the periodic boundary, which leads to a small equivalent load impedance ($Z_L^{\pm} = 0$) and a large input impedance ($|Z_T| \to \infty$). This implies that the reflection coefficient in Equation (5-3) is effectively reduced to $r_H = \left[iZ_S - Z_0 \tan(\beta_S t_M)\right] / \left[iZ_S + Z_0 \tan(\beta_S t_M)\right];$, producing unitary reflectivity $|r_H|^2 = 1$. Such condition holds for arbitrary conditions, independent of the incident angle, at the symmetric resonance of the TL unit cell. This is consistent with strongly resonant metasurfaces with angular independent reflectivity based on the resonance of their individual constitutive elements [94-96].

In addition, a different, quasi-omnidirectional reflection condition takes place in our geometry at the anti-symmetric resonance of the TL unit cell. In the lossless case, the field ratio becomes $\gamma_H^{\pm} = -1$ for this anti-symmetric resonance under the condition $\beta_D l = m\pi$ (with m being an integer), following a zero in the magnetic field at the periodic boundaries. Under such circumstance, we obtain a large equivalent load impedance $Z_L^{\pm}$, which ensures again a large input impedance $|Z_T| \to \infty$. Interestingly, this anti-symmetric resonance condition also leads to unity reflectivity ($|r_H|^2 = 1$), ideally offering another bandgap at a different frequency for the proposed geometry. Note, however, that this reflection condition is weakly dependent on the angle, as it can be excited only at oblique illumination $\theta > 0°$ to support an anti-symmetric field distribution ($\gamma_H^{\pm} = -1$), as predicted from Equation (5-2).

5.3 SIMULATION RESULTS

In order to demonstrate the proposed bandgap mechanisms, we compare full-wave numerical simulations based on CST Microwave Studio™ to our analytical model.

In Figure 5-2, we analyze the effect on the angular TM transmission power spectra of the MDM waveguide. We choose a metal thickness t_M =100 nm, a slit width $w_S = 40$ nm, a grating period $p = 160$ nm and various thicknesses of the dielectric layer ($w_D = 0$ nm in absence of the central waveguide), showing that the bandgap mechanism is essentially governed by the coupled resonance modes in the transverse direction, as predicted by our theory. Throughout this letter, relatively large slit apertures w_S compared to the array periodicity p are considered, in order to take advantage of semi-transparent gratings that allow a clearer display of the presented bandgap response. In our analytical model and simulations, we fully consider the finite conductivity of silver [47] and the corresponding dispersion of the supported guided modes. It is obvious that our TL model does not take into account the higher-order reactive modes at the grating entrance and exit apertures, since these effects are predicted to be small for small periodicity $p < \lambda/2$. These are fully taken into account by our numerical simulations, confirming the accuracy of our analytical model, especially at lower frequencies.

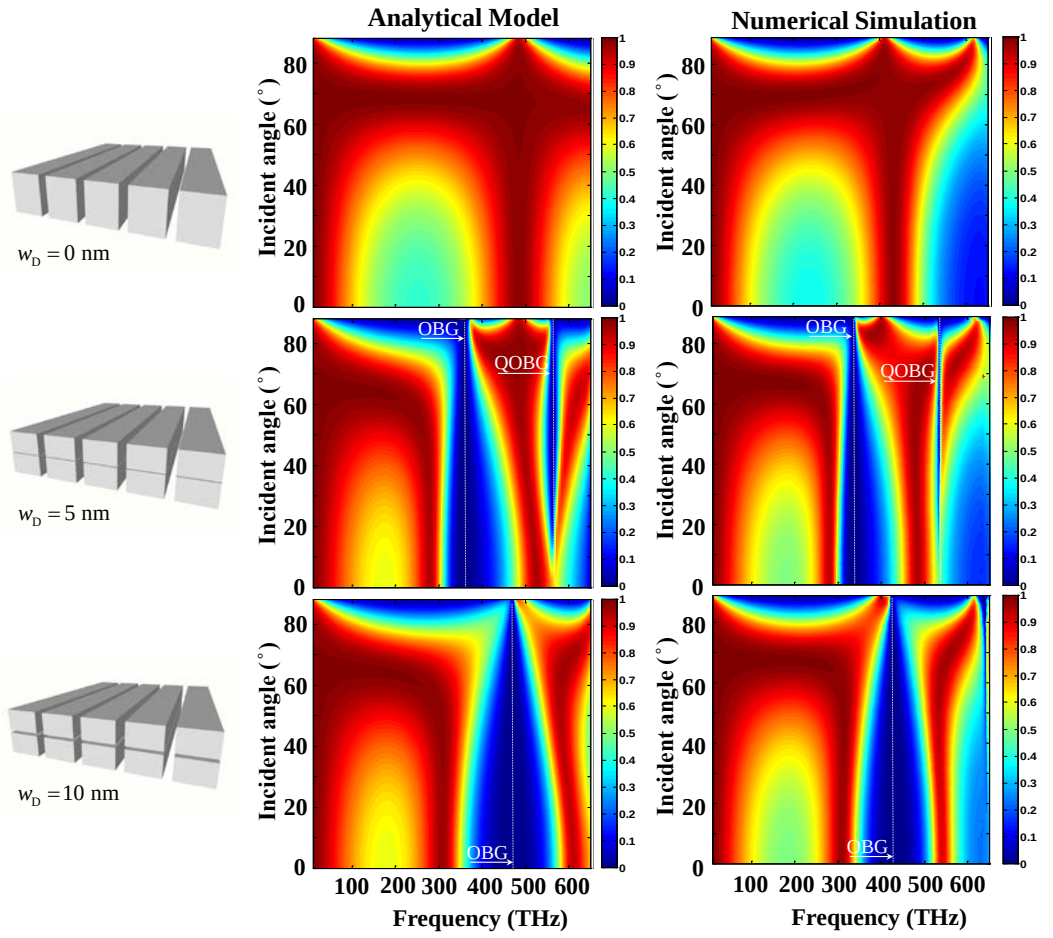

Figure 5-2: Power transmission spectra for $w_S = 40$ nm, $t_M = 100$ nm, $p = 160$ nm, and $w_D = 0$ nm (top row), $w_D = 5$ nm (center row), and $w_D = 10$ nm (bottom row). OBG and QOBG stand for omnidirectional and quasi-omnidirectional bandgap, respectively.

Towards the higher end of the considered spectrum these effects become relatively more important and the TL model loses part of its accuracy, as visible in Figure 5-2, due to the larger ratio between transverse periodicity and wavelength. Also some minor discrepancy is found in the resonant modal wavenumber between our analytical model and numerical simulations in this frequency regime; however, our model still

captures all the main mechanisms behind the generation of two clear bandgaps over the wide frequency range of interest as soon as a dielectric transverse slit is opened in the metallic layer, as we discuss next.

For the case without MDM waveguide (top row of Figure 5-2), a typical extraordinary optical transmission (EOT) effect is observed. In this case, vertical (narrowband) transmission bands associated to conventional Fabry-Perot resonances and horizontal (nonresonant) transmission bands associated to "plasmonic Brewster angle" funneling [95] are observed. In contrast, the transmission becomes significantly more complex once a dielectric slit is added in this geometry, and significant resonant reflection can be observed in the other panels. In the center row of Figure 5-2, the omnidirectional bandgap response is displayed at the first resonant frequency $f = 385$ THz, corresponding to the symmetric resonance mode $\mathrm{Re}\left[\beta_{\mathrm{D}}\right] l = \pi / 2$. For arbitrary incident angle, literally from normal to 90°, the configuration under investigation shows an effective suppression of light transmission. Similarly, a quasi-omnidirectional bandgap response is noticed for oblique incidence at the second resonance frequency $f = 564$ THz, corresponding to the anti-symmetric resonance mode $\mathrm{Re}\left[\beta_{\mathrm{D}}\right] l = \pi$. This second reflection band is effective within the range of incident angles from 12° to 90°. The predicted transmission minima of both analytical models and numerical simulations are marked in each panel, confirming the validity of our model.

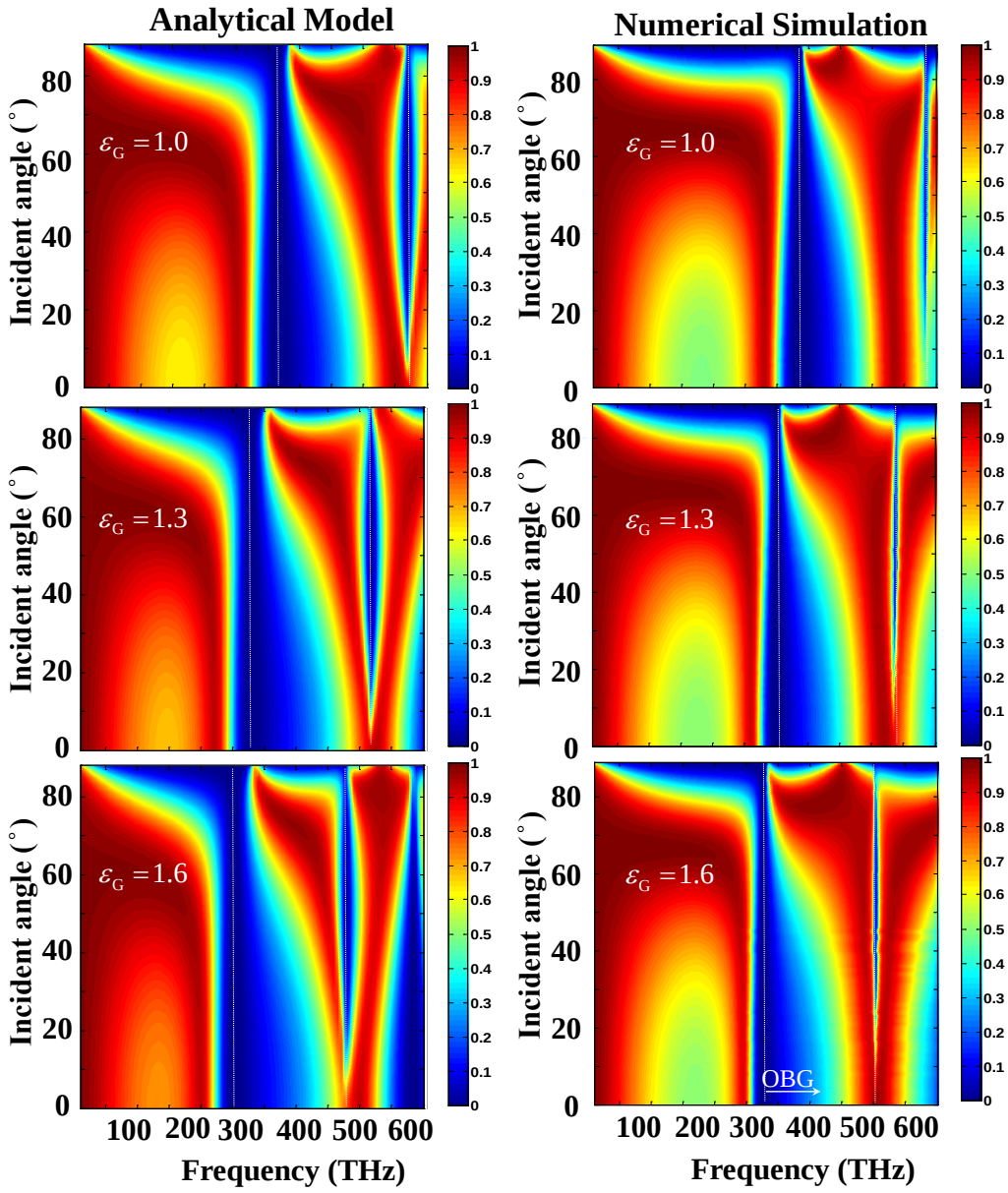

Figure 5-3: Tunable bandgap responses of waveguide network with $w_S = 40$ nm, $t_M = 100$ nm, $p = 160$ nm, and $w_D = 5$ nm but with different filling material ε_G in junction waveguides.

For waveguides with a wider dielectric layer ($w_D = 10$ nm), we observe a shift to higher frequencies of these bandgaps, due to faster modal propagation in the

corresponding MDM waveguide $\beta_D(w_D = 10\text{ nm}) < \beta_D(w_D = 5\text{ nm})$. Such tunable nature of the plasmonic bandgap response may be further demonstrated by changing the material filling the MDM waveguide to modulate the propagation in the transverse direction. In Figure 5-3, we show tunable bandgap response corresponding to an index change in the filling material, which may be of interest for sensing purposes.

In Figure 5-4, we consider a different geometry, with parameters w_S =40 nm, p =200 nm, w_D =5 nm and different metal thicknesses t_M to emphasize the fact that bandgap response is solely determined by the unit cell resonances outlined above. Essentially, the MDM waveguide opens a Fano interference in the modal dispersion of the grating, allowing sharp resonant reflection, weakly dependent on the incident angle.

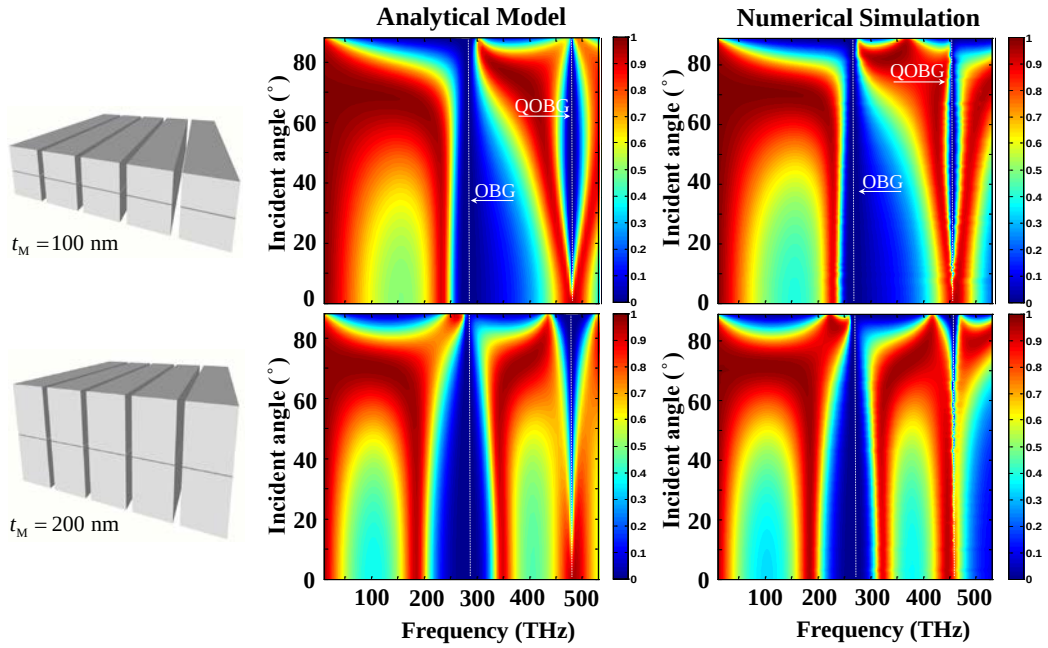

Figure 5-4: Angular power transmission spectra for $w_S = 40$ nm, $w_D = 5$ nm, $p = 200$ nm, and various metal thicknesses: $t_M = 100$ nm (top row) and $t_M = 200$ nm . (bottom row).

As visible in both our analytical results and numerical simulations, the transmission minima (shown as dotted lines) ensure a unique resonant bandgap response, independent of t_M . We also highlight the difference between the symmetric (omnidirectional) and asymmetric (quasi-omnidirectional) bandgap by analyzing the field distribution of the standing waves in the E-plane waveguide junction. For this purpose, we analyze the geometry of Figure 5-4 (bottom row) excited at near grazing angle ($\theta = 75°$)to verify the two resonance reflection mechanisms as a function of frequency.

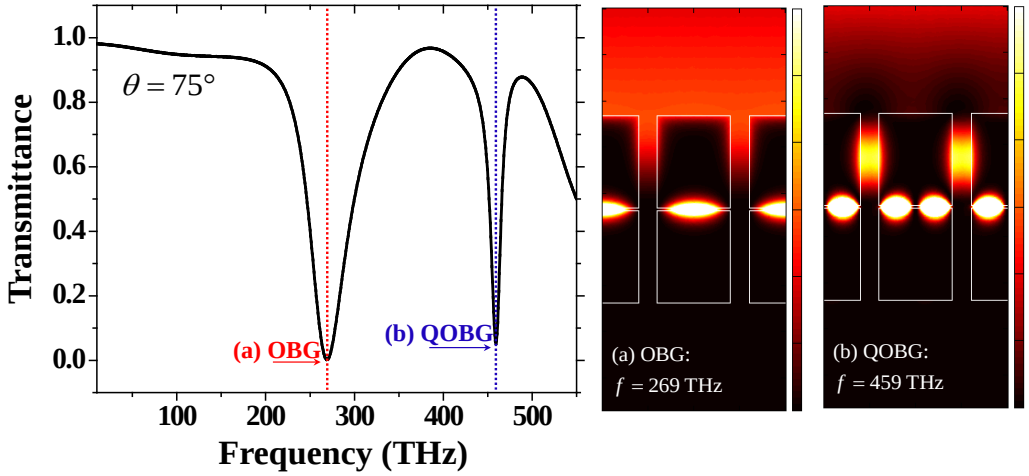

Figure 5-5: Power transmission spectrum for $w_S = 40$ nm, $w_D = 5$ nm, $p = 200$ nm, and $t_M = 200$ nm for oblique incidence ($\theta = 75°$), and magnetic energy density distribution for (a) omnidirectional bandgap and (b) quasi-omnidirectional bandgap.

Figure 5-5 shows for this geometry the presence of two resonant dips, associated with the two different resonant modes, consistent with Figure 5-4. In Figure 5-5(a) and 5-5(b), we compare the magnetic energy density distribution $|H_y|^2$ at the two dips. We see that the energy is confined in the transverse direction, with null fields at the boundaries of each unit cell (at the slit center), ensuring the formation of an effective impedance barrier

($|Z_T| \to \infty$) in both cases, which sustains the resonance. The omnidirectional (symmetric) resonance is the first-order resonance of the unit cell, while at higher-frequencies, for a shorter guided wavelength, we hit an anti-symmetric resonance with an additional null field at the center of the unit cell. It is also noticed that the phase of the reflected wave at the entrance of the slits is different at the two resonance frequencies, and it is essentially controlled by the modulation of β_S and t_M without affecting the bandgap responses, following Equationo (5-2) This may be interesting to realize high-impedance surfaces, or locally modulate the reflection coefficient in the transverse plane.

5.4 TRANSMISSION THROUGH GRATINGS IN MIM SCREEN

The transmission peaks observed in Figure 5-4 do not necessarily all rely on a resonance of the individual unit cell. Some transmission peaks relocate as a function of the position of the resonant reflection modes discussed above, and they are based on modal impedance matching with the reactive impedance of the central waveguide, generalizing the results previously presented in Ref. [95]. This type of transmission peaks is especially found around the points in which the reactive impedance on the E-plane junction (stub impedance) compensates the input reactance seen at the center of junction toward the slit aperture.

To verify this concept, we define two sets of input impedance seen from the series junction $Z_{STUB}^{\pm} = Z_D\left[Z_L^{\pm} - iZ_D \tan(\beta_D l)\right] / \left[Z_D - iZ_L^{\pm} \tan(\beta_D l)\right]$ (+ for right-handed and – for left-handed stub in Figure 5-1 (1) and $Z_{IN} = Z_S\left[Z_0 - iZ_S \tan(\beta_S t_M)\right] / \left[Z_S - iZ_0 \tan(\beta_S t_M)\right]$ (input impedance toward slit opening). Since the off-resonance input resistance $\mathrm{Re}\left[Z_{STUB}^{+} + Z_{STUB}^{-}\right]$ is very low, the condition for maximum power transfer through the grating reduces to $\mathrm{Im}\left[Z_{STUB}^{\pm}\right] + 2\,\mathrm{Im}\left[Z_{IN}\right] = 0$. In Fig. 5-6, we show the condition for maximum power

transfer and corresponding distribution of magnetic energy density for the geometry of Figure 5-5 for normal incidence, to further verify how the modal impedance matching in the junction waveguide affects the transmission peaks.

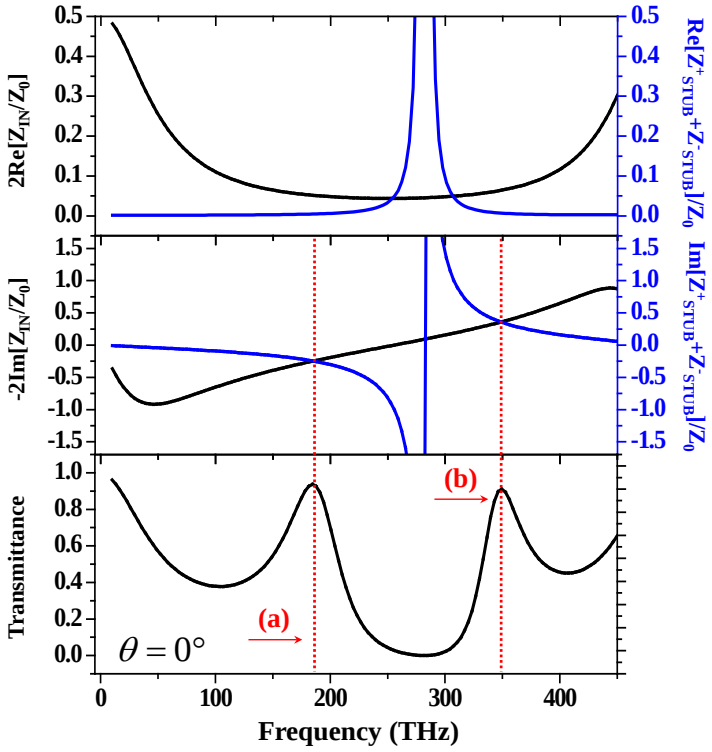

Figure 5-6: Impedance matching conditions for maximum power transfer through the thin plasmonic grating geometry with $w_S = 40$ nm, $w_D = 5$ nm, $p = 200$ nm, and $t_M = 200$ nm for normal incidence. Peak transmissions (a) at $f = 184$ THz, and (b) at $f = 324$ THz are obtained when the reactance of input impedance toward slit opening Z_{IN} is compensated by stub impedance $Z_{STUB}^{\pm}$.

Similar transmission mechanisms are commonly used in microwave engineering applications, referred as stub-matched transmission [92]. Transmission peaks, visible as

vertical lines in Figure 5-4 and relatively independent on the angle, are shifted to some other frequencies as a function of t_M.

5.5 Extended Application: Angle-insensitive Bandgap Response on Thin Film Gratings

It is shown how the two resonances have formed on E-plane of wave propagation relevant to the bandgap phenomena and also demonstrated how the bandgap mechanism is applied to the proposed geometry. Although such bandgap mechanism is frequently used in the longer wavelength applications such as microwave engineering and antenna engineering, only limit numbers of literatures have devoted for optical frequency applications on the modeling of such band suppression phenomenon while counting on the complex numerical calculations. In this regard, our modeling methodology would take benefits as a useful tool for predicting the bandgap response of periodic geometry supporting the guidance and resonance on E-Plane. In this section, we benefit our TL modeling methodology to anticipate whether the geometry supports the omnidirectional bandgap mechanism. Following that, we consider the one well known bandgap geometry which consists of gratings in thin metal screen as shown in Figure 5-7.

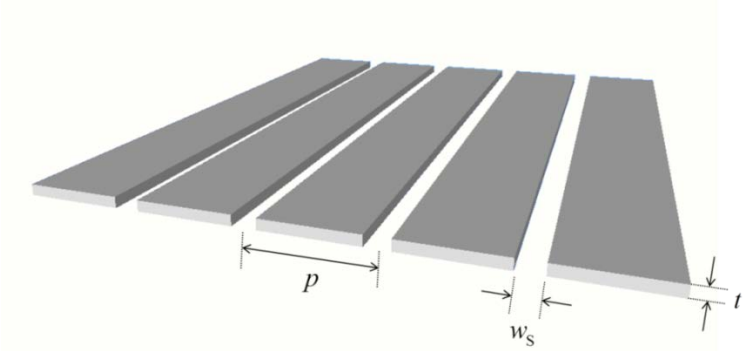

Figure 5-7: 2D plasmonic gratings in thin Ag film. p is the period, w_S is the slit width, and t is the thickness of screen. Similar to the configuration in Figure 5-1, we consider the TM waves incident on this geometry in which the magnetic fields are parallel to the ruling direction of gratings.

Since thin metal film supports modal wave propagations along its interfaces, for impinging TM light it would be possible to form a coupled resonance modes on E-plane by having horizontal waveguide modes thus it may offer an omnidirectional bandgap responses as we discuss in the previous sections. To prove this, we first carry out numerical simulations to show how the gratings in thin film would affect to the light transmission. In Figure 5-8, we show the numerical simulations of angular transmittance of bulk film (Figure 5-8(a)) and screen with slit-gratings (Figure 5-8(b)). At optical frequency where the frequency is higher than the plasma frequency of metal, it is well known that thin bulk metal film is semi-transparent not only due to the finite thin profile but also due to the dielectric property associated with plasma frequency. Although lots of applications at optical frequency are counting on this property, however such semi-transparency is no longer being achieved especially for the lower frequency application with a bulk metal screen since the dielectric properties of metal at lower frequency

becomes more “metallic” due to the lack of oscillatory bound electrons being populated. This corresponds to the high reflectivity of bulk metal screen for impinging light at lower frequency of operation as seen in Figure 5-8(a). Unlike the bulk thin film, the angular transmission is clearly distinctive that the periodically patterned metallic film is highly transparent at lower optical frequency as reported in somewhere else. As long as the film is considerably thinner than the wavelength of operation ($t << \lambda$), large portion of optical energy will be transmitted through the patterned screen without being affected by modal resonances along slits. Also it is noticed that the thin metal screen with periodic slit-gratings shows strong suppression at some frequencies which may be associated with bandgap responses induced by coupled resonance modes.

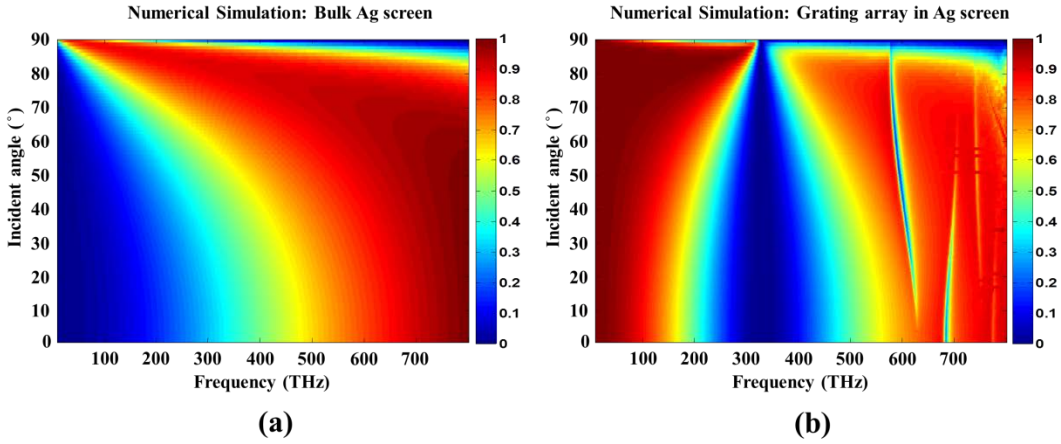

Figure 5-8: Angular power transmission spectra of (a) thin bulk screen ($t = 5$ nm), and (b) periodic gratings in thin film screen for $w_S = 20$ nm, $t = 5$ nm, and $p = 200$ nm.

5.6 Experimental Demonstration of Bandgap Response

In the previous section, we explore theoretical approaches to show how omnidirectional bandgap response is formed. Based on the geometry where the coupled resonance modes along the transverse direction are supported, it is shown that the light transmission is effectively suppressed for omnidirectional radiation. Extended from theoretical studies, in this section, we show that how the bandgap mechanism is experimentally demonstrated. For the realization of geometry in Figure 5-1, we consider the realistic configuration as shown in Figure 5-10 in which the MIM screen is realized over the BK7 glass substrate and we chose to adopt nanofabrication technologies capable of producing sub-100 nm feature size to realize nanometer-scale array geometry. First, commercially available BK7 glass substrate was prepared and cleaned through "piranha (H_2SO_4+H_2O_2) cleaning" procedure in order to completely remove organic residues on the substrate. The cleaned substrate was then completely dried on the hot plate at 200 ºC and then allowed to cool. Secondly, the MDM film Ag/SiO_2/Ag (50 nm/50 nm/50 nm) was evaporated on the substrate aided by E-beam. Note that 2.5 nm thick Ge layer was used to serve as a wetting layer [77, 97] to enhance adhesion and surface quality of MDM film. An array of slit-gratings for different periods were defined in MDM film by focused ion beam (FEI SEM/FIB dual beam, FEI Corp., OR, USA) milling. The milled slit had a width of 55~70 nm supporting the fundamental modal propagation inside.

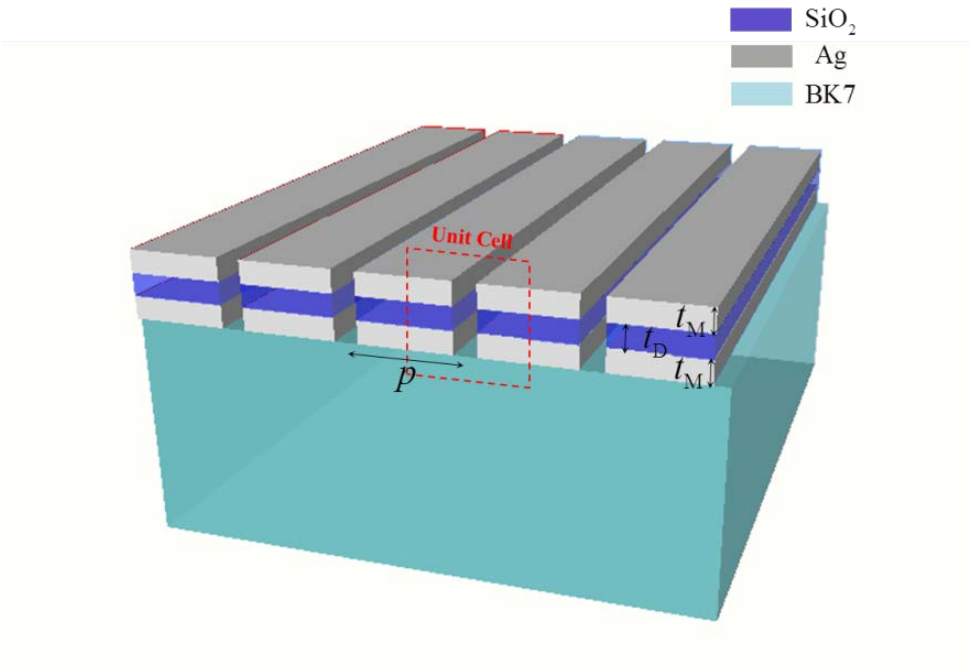

Figure 5-10: The proposed geometry: a 2D plasmonic grating in MDM screen realized over the BK7 substrate.

The light transmission through the fabricated device was then characterized with a custom optical setup allowing to measure the spectrum for wide angle coverage of incident light. In order to maximize the acceptance angle of the objective lens (Plan N 100X 1.25 N.A., Olympus), the index matching fluid (n = 1.52 at $\lambda = 633\,\text{nm}$) was dispensed to fill the gap between the objective lens and the device. The transmission spectrum was then resolved by diffraction grating (150 g/mm with blaze wavelength of 500 nm) and recorded on linear array CCD (PIXIS, Princeton Instruments) as shown in Figure 5-11. For the wide-angle illumination of device, Abbe condenser (1.25 N.A.) coupled with broadband light source (halogen/tungsten lamp) was used.

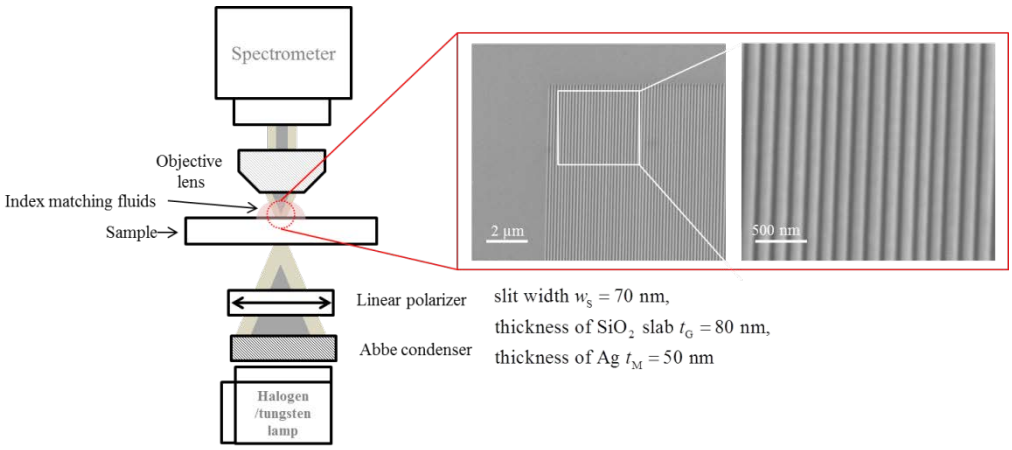

Figure 5-11: Experimental setup for the bandgap measurement. The insets are SEM images of slit-gratings in MDM ($Ag/SiO_2/Ag$) screen. Both objective lens and the device are immersed in index-matching medium (n=1.52).

The transmission spectrum showing the bandgap responses at the resonant frequencies were captured for different design parameters ($p = 180$ nm and $p = 200$ nm). As seen in Figure 5-12, the omnidirectional bandgap responses associated with the symmetric coupled resonance mode ($\mathrm{Re}\left[\beta_D\left(p - w_S\right)\right] = \pi$) along the horizontal MDM waveguide at 621 nm and 689 nm are clearly observed. It is worth to note that we also observe quasi-omnidirectional bandgap like responses at the wavelength of about 453 nm and 495 nm, but unfortunately, it was not clearly seen due to the limit of optical measurement setup only allowing wide angle coverage for spectrum recording but controllability of illumination/observation angle. Further experimental verification on angular transmission analysis would be our future goal in order to more rigorously prove the omnidirectional/quasi-omnidirectioanl bandgap responses offered by the proposed geometry.

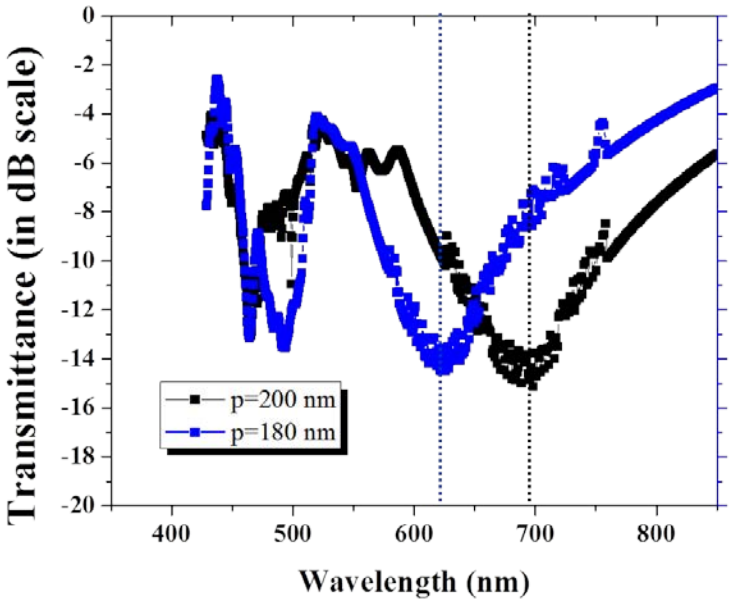

Figure 5-12: Transmission spectrum of the device in Figure 5-10 for $p = 180$ nm (blue curve), and $p = 200$ nm (black curve).

5.6 CONCLUSIONS

It is seen how the two resonances have remarkably different density distributions, based on different localized resonant modes in the MDM geometry. In conclusion, we have introduced a plasmonic grating structure based on a two-dimensional MDM plasmonic waveguide network that may provide efficient suppression of light transmission with distinctive omnidirectional sharp bandgaps. We have presented a powerful TL model that allows predicting all the main mechanisms behind this phenomenon, shown to be rather independent to the incident angle but highly selective to the frequency of operation. With the use of moderately wide slit arrays compared to the periodicity and the waveguide width, we have demonstrated efficient control of both transmission and band suppression through the structure. We stress that this band suppression phenomenon is not related to the photonic absorption associated with the

lossy nature of metal at optical frequency. Although this assertion is already pointed out in the TL modeling, it is worth to note again, in order to differentiate the bandgap response from the typical energy absorption phenomena. For this, we consider the geometry being composed of perfect electric conductor (PEC) in which the no energy absorption occurs.

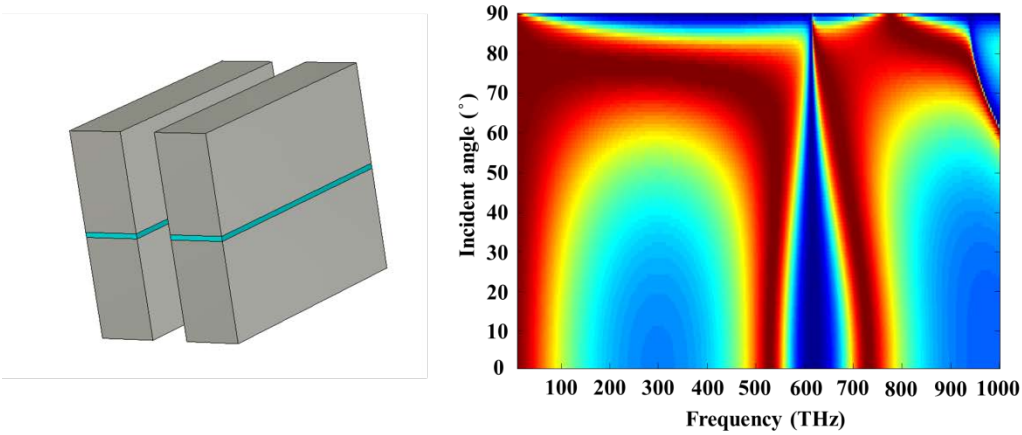

Figure 5-13 Angular power transmission spectra of periodic gratings in PEC film screen for $w_S = 40$ nm, $p = 160$ nm, and $w_G = 5$ nm. Transverse MDM waveguide is filled with $\varepsilon_r = 4$ medium.

Similar to the plasmonic bandgap geometry in Figure 5-1, omnidirectional bandsuppression is noticed in Figure 5-13 as expected from our models presented throughout this chapter. In addition, we also present the preliminary demonstration of bandgap response by realizing the proposed geometry with nano fabrication technologies. With the optical measurement setup allowing the spectrum measurement for wide-angle coverage, it has been shown that an array of slit-gratings in MDM screen can provide effective band suppression. The presented bandgap mechanism may be applied to the

development of novel nanophotonic filters, such as reflection color filters or quantum-dot based LEDs.

Chapter 6: Tunable Transmission through Grating Array in MIM Screen

In this chapter, we show experimental studies on the grating geometry described in the Chapter 5. We validate that the slit-based gratings in MIM screen may support efficient transmission of light based on the impedance matching conditions which may be extended for the use of filter applications and sensing applications. As a preliminary step, an array of gratings in MIM screen was fabricated and characterized for demonstrating tunable transmission phenomenon. Specifically, the transmission spectra for various slit-grating designs are analyzed while potential ways of tuning the light transmission are studied. Following preliminary demonstration of tunable transmission for various design parameters and controlled bulk dielectric indices, we show that the transmission can be also controlled by modifying the local index of medium surrounding the geometry which may be further extended for biosensing platform.

6.1 INTRODUCTION

Recent progress in nanophotonics has been made with a special emphasis on the efficient controls of photons. Especially, tailoring the electromagnetic transmission through gratings is an actively studied subject of interest in the optical frequency applications. Since the first re-discovery of extraordinary transmission phenomena in array geometry [53], the various mechanism of such enhanced light transmission have been proposed and verified [53, 98-100]. Being based on the previous findings [49, 53, 78, 80, 93, 98-105], we further investigate the new capability of the nano-patterned metal-dielectric-metal film with gratings for use as plasmonic color filter arrays having spectral tunability. This study in this chapter would represent an attractive potential approach for on-chip color filters, which are vital components for sensors, display

applications, and other optical measurement instrumentation. In the previous chapter, we discuss the light transmission through patterned MIM screen being ruled by the impedance matching condition where the maximum optical power transfer occurs. It is noted that effective transmission through gratings in MDM screen is placed adjacent to the resonant frequencies; however, this is not related to the resonant phenomena on E-plane of light transmission but associated with the reactance compensations which is also known as impedance matching condition for lower frequency applications. Following previous findings described throughout chapter 5, we propose and experimentally demonstrate the tunable color filter consisting of an array of gratings in metal screen. Specifically, we show that transmission of light can be manipulated by controlling the index of surrounding medium. First, we study that tunable light transmission from gratings which is tailored by dielectric property of bulk surrounding medium. Following this, we also show how the local change of dielectric indices can affect to the light transmission.

6.2 TUNABLE TRANSMISSION MECHANISM

In this chapter, it was studied that the light transmission through the opaque metal screen can be enhanced and spectrally tailored [98-100] through proper designs of gratings perforated in the screen. Being based on its resonant modes or the impedance matching conditions, we may achieve the desired spectral response of transmitted light through those gratings. Following the concept of tailored transmission spectrum by the metal geometry (especially plasmonic geometry at optical frequency), we explore the possible tunability of light transmission through the manipulation of bulk or local dielectric properties. For this purpose, we consider the geometry that we studied in the previous chapter consisting of periodic gratings in the metal screens separated by thin

dielectric slab. In details, we assume that the two metal screens are separated by the SiO_2 slab and slit gratings are perforated through those MIM screen. Such nanopatterned metal screens are supported by the BK7 substrate as shown in Figure 6-1.

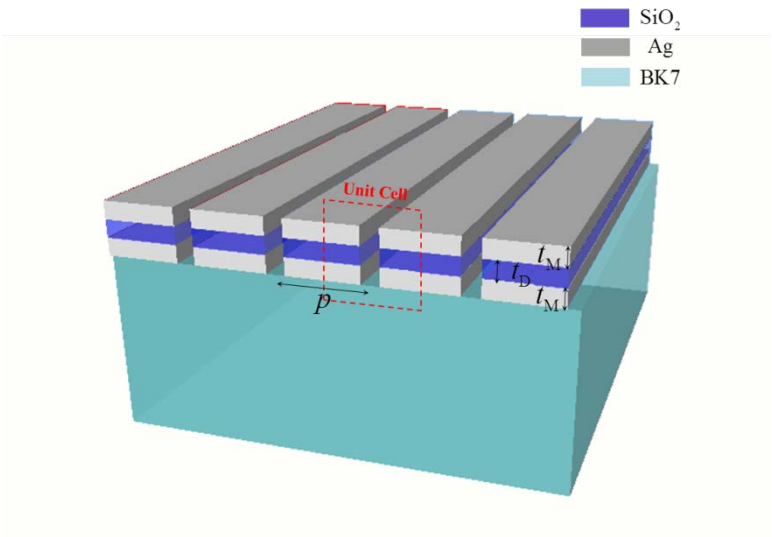

Figure 6-1: The proposed geometry: p is the period, t_M is the thickness of metal, and t_D is the thickness of SiO_2 slab. Throughout this chapter, we investigate the geometry for $t_M = t_D = 80$ nm, and various p. We also consider the effect of bulk or local variation of dielectric property on the light transmission property.

Using the geometry shown in Figure 6-1, we explore the light transmission through the gratings for both scenarios when bulk and local dielectric index around the geometry is changed. Such tailoring of dielectric property may be achieved simply through dispense of fluids on the geometry, or utilization of chemical bond which allows the binding of specific chemical to target binding target. Details of each scenario will be presented in the following sections. The primary goal of herein is to experimentally demonstrate the tunable light transmission mediated by controlling dielectric index around the device in Figure 6-1. Figure 6-2(a) shows the transmission-line (TL) model of

the proposed geometry in Figure 6-1, which can be further simplified to the circuit model in Figure 6-2(b).

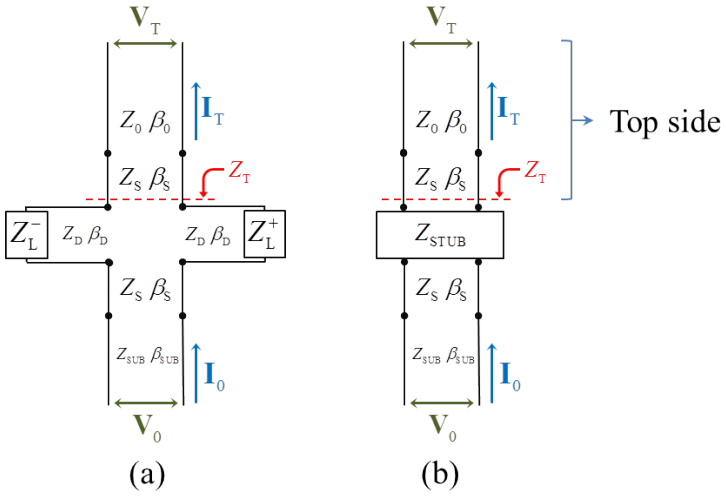

Figure 6-2: (a) Equivalent circuit of the proposed geometry in Figure 6-1. (b) Simplified equivalent circuit of 6-2(a) with series junction impedance Z_{STUB}. Z_{SUB} is the impedance of substrate defined as $Z_{\mathrm{SUB}} = p\beta_{\mathrm{SUB}}/\omega\varepsilon_0$.

The series junction impedance Z_{STUB} can be defined as the sum of stub impedances as

$$Z_{\mathrm{STUB}} = Z_{\mathrm{D}}\left[Z_{\mathrm{L}}^{+} - iZ_{\mathrm{D}}\tan\left(\beta_{\mathrm{D}}l\right)\right]\Big/\left[Z_{\mathrm{D}} - iZ_{\mathrm{L}}^{+}\tan\left(\beta_{\mathrm{D}}l\right)\right] + Z_{\mathrm{D}}\left[Z_{\mathrm{L}}^{-} - iZ_{\mathrm{D}}\tan\left(\beta_{\mathrm{D}}l\right)\right]\Big/\left[Z_{\mathrm{D}} - iZ_{\mathrm{L}}^{-}\tan\left(\beta_{\mathrm{D}}l\right)\right], \quad (6\text{-}1)$$

where $l = \left(p - w_{\mathrm{S}}\right)/2$. Important optical property associated with Z_{STUB} is that this stub impedance can be either capacitive or inductive depending on the stub length l, frequency f_0, and the incident angle θ as described in the equation 5-2. This property directly corresponds to the fact that complex mechanism with various tuning factors should be considered to realize the effective transmission; however, the general rule is can be found by considering impedance matching conditions where reactance on the path to optical power transfer is compensated to minimal value. Depending on the reactive

impedance compensation condition, the frequency where effective transmission occurs will vary. For the proposed geometry, there are two physical locations where the reactive impedance can be modified: the slit in the top side associated with Z_{STUB} and slit Z_{S} loaded with surrounding medium Z_0. By tailoring complex impedance of target places, we may achieve to introduce tunable transmission of light through the proposed geometry. For the simpler analysis, one may consider TEM impinging waves (incident normal $\theta = 0°$ on the MDM screen) so that the equation (6-1) can be simplified to $Z_{\mathrm{STUB}} = -2iZ_{\mathrm{D}} \tan\left(\beta_{\mathrm{D}} l\right)$. Under this simplified condition, the impedance imposed by the stub is purely reactive and can be compensated by tuning the top side impedance in Figure 6-2 including the slit impedance. In order to achieve such tailoring impedance and in turn tunable transmission in temporal domain, one may control the dielectric index of the bulk surrounding medium or the local index inside the slit. By such simple treatments, one may achieve tunable transmission of light from the proposed geometry. For controlling bulk dielectric index, we uses commercially available index matching fluids (Cargille Labs) and aminosilane coupling agent, 3-aminopropyltriethoxysilane (APTES) [106-108], is used to create thin layer of index control film on both exposed silver and SiO_2 surfaces on the geometry.

6.3 BULK INDEX-MEDIATED TUNABLE TRANSMISSION

The proposed geometry was built with nano fabrication technology. Details of the fabrication process are described in followings. First, commercially available BK7 glass substrate was cleaved and cleaned through “piranha (H2SO4+H2O2) cleaning” procedure in order to completely remove organic residues on the substrate. The cleaned substrate was then completely dried on the hot plate at 200 ºC and allowed to cool. This cleaning process is essential for the quality film deposition on the BK7 substrate. Secondly, the

MDM film Ag/SiO2/Ag (50 nm/80 nm/50 nm) was evaporated on the substrate aided by E-beam. Note that 3 nm thick Ge layer was used to serve as a wetting layer [77, 97] to enhance adhesion and surface quality of MDM film. An array of slit-gratings perforated in MDM film were defined by focused ion beam (FEI SEM/FIB dual beam, FEI Corp., OR, USA) milling. The milled slit had a width of 40~50 nm and devices having various periods were fabricated. To observe the normal transmission from the device, typical microscope setup was used and spectrum of transmitted light was resolved by diffraction gratings and in turn recorded by line-array CCD. Detailed configurations of measurement setup are found in Figure 6-3.

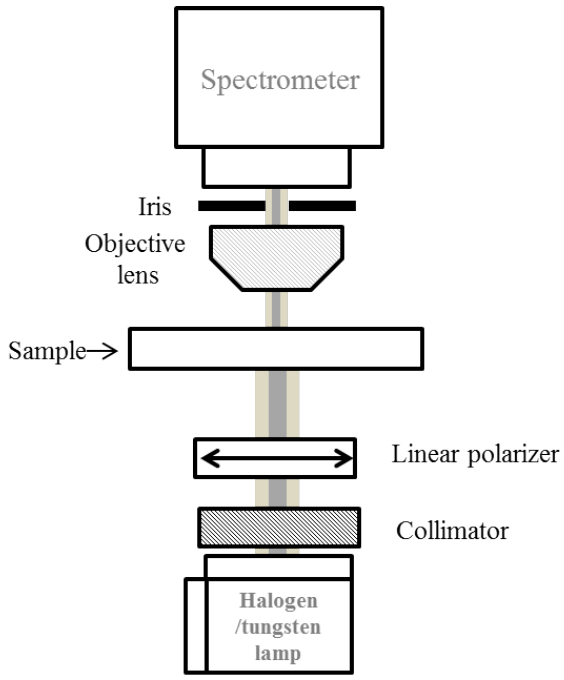

Figure 6-3: Schematic diagram of experimental setup. Long-working distance objective lens (Olympus LMPlan X20/0.4) with closed iris wass used to collect transmitted light for narrow acceptance angle.

Wide spectrum for light illumination was generated by the discharge lamps (halogen/tungsten lamp) and transmitted light was collected by long-range objective lens (Olympus LMPlan X20/0.4) with closed iris to acquire sharp acceptance angle so that only normal light transmission through the device could be collected by the optics. Figure 6-4 shows the SEM images of one fabricated slit-gratings perforated in MDM film with varying periodicity ($p = 350$ nm ~ 150 nm).

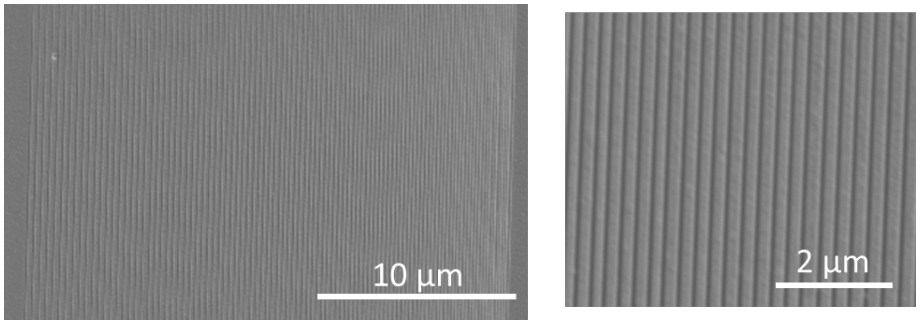

Figure 6-4: SEM images of fabricated gratings in MDM ($Ag/SiO_2/Ag$) screen. The supporting substrate is BK7 glass. Silt-gratings were perforated in MDM film with various periodicity from 350 nm (left) to 150 nm (right).

The fabricated devices were first characterized on the microscope and images of transmitted light were then recorded for various surrounding indices. To precisely control the index of surrounding dielectric medium, we use commercially available index matching fluids (Cargille Labs). Figure 6-5 shows the microscope images of devices illuminated by white light source for various dielectric indices (n = 1.0 (air) ~ 1.54) of surrounding medium. For the case in which no surrounding medium is applied (n = 1.0) (in the top left of Figure 6-5), it is noticed that only small portion of light can penetrate through the gratings especially for the large periodicity in the visible wavelength range. Such low transmission efficiency at larger periodicity is related to the significant impedance mismatch failing to compensate the reactance in the slit-grating geometry. In

contrast, transmission efficiency was improved as the index of surrounding medium increases which can be expected from the Equation (6-1).

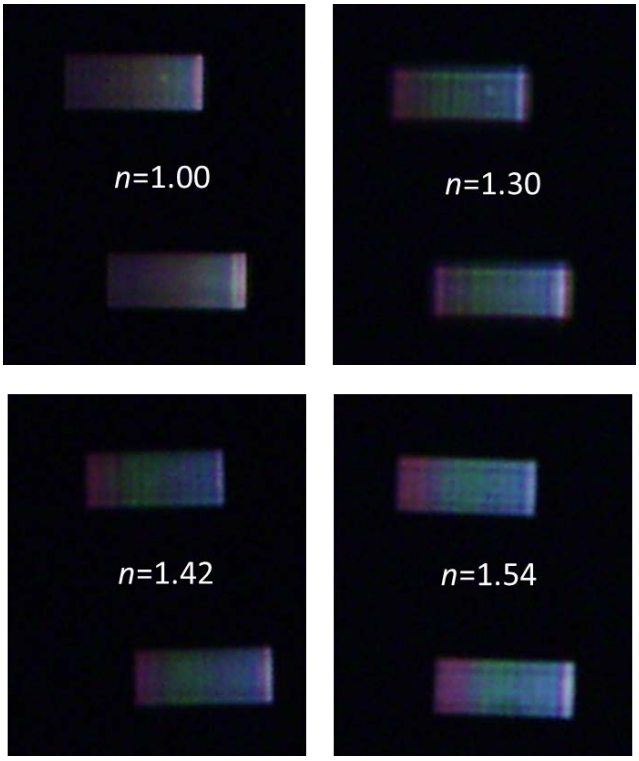

Figure 6-5: Microscope images of light transmission through the devices in Figure 6-4 for various surrounding indices: (top left) n = 1.00, (top right) n = 1.30, (bottom left) n = 1.42, and (bottom right) n = 1.54.

For qualitative spectrum analysis, devices for different periodicity were fabricated; and their transmission spectrums were measured and compared with numerical simulation results. Figure 6-6 shows the normal transmission spectrums for devices having various periodicities (p = 200, 250, and 300 nm). In general, as it expected from the equation (6-1), the smaller periodicity corresponds to the effective light transmission at lower wavelength. It is noticed that the light transmission red-shifts for higher refractive index of surrounding medium.

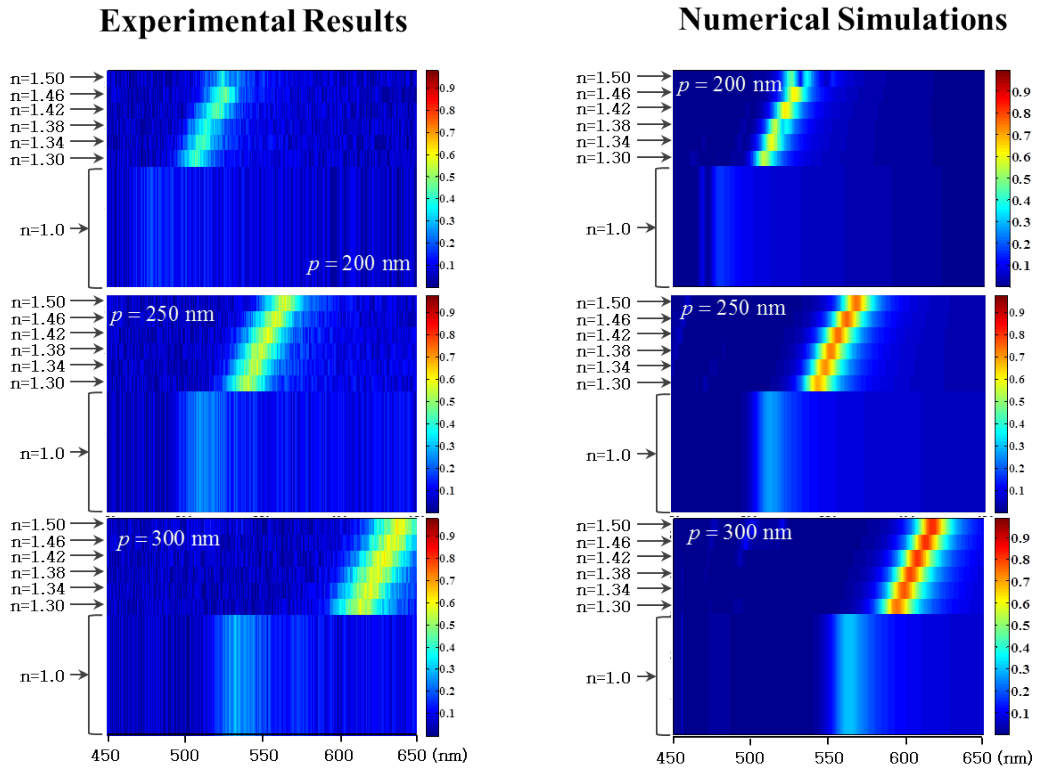

Figure 6-6: Normal transmission spectrum for various periodicities and surrounding indices: (left column) experimental results and (right column) numerical simulations.

6.4 TUNABLE LIGHT TRANSMISSION BY LOCAL INDEX MODULATION INSPIRED BY BIO-SENSING APPLICATION

We have investigated tunable light transmission mechanism mediated by bulk index modification and its experimental demonstrations. By tailoring the index of surrounding medium from n =1.30 to n = 1.54, more than 40 nm shift of transmission spectrum could be achieved. Following this, we further investigate the sensing capability of proposed geometry for the local index changes to see whether the proposed geometry can offer effective sensing mechanism for potential biosensing application. . Although such transmission shift by local index change may not be significant for applications

which utilize spectrum shift as a sensing measure, if the intensity change upon the presence of sensing material is significant enough, then one can still find the sensing platform based on the variation of transmission intensity. For this, we consider the geometry in Figure 6-1 for the detection of local index changes. In order to provide local dielectric index changes, we utilize the self-assembly method which is also known as silanization to create thin dielectric layer on binding surfaces. As a binding agent, we choose aminosilane coupling agent, 3-aminopropyltriethoxysilane (APTES) [106-108] to form covalently-bound thin layer of index control film on both exposed hydroxylated surfaces including silver and SiO_2 on the geometry. For the accurate controls of film profile assembled on target surfaces, we carried out the film characterizations on bare target surfaces with atomic force microscopy (AFM) for various binding conditions as shown in Table 6-1.

No.	Concentration	Solution (temp.)	Binding Surface	Immersion Time	RMS Profile
1	> 2%	Toluene (RT)	SiO_2	24 h	~ 31 nm
2	0.5 %	Toluene (RT)	SiO_2	24 h	~ 36 nm
3	0.5 %	Toluene (RT)	SiO_2	12 h	~ 24 nm
4	0.5 %	Toluene (RT)	SiO_2	6 h	~ 24 nm
5	0.5 %	Toluene (RT)	SiO_2	4 h	~ 12 nm
6	1 %	Toluene (RT)	SiO_2	1.5 h	~ 10 nm
7	1 %	Toluene (RT)	SiO_2	1 h	~ 6 nm
8	1 %	Toluene (RT)	SiO_2	0.75 h	~ 4 nm
9	0.5 %	Toluene (RT)	Ag	24 h	~ 30 nm
10	0.5 %	Toluene (RT)	Ag	12 h	~ 24 nm
11	0.5 %	Toluene (RT)	Ag	6 h	~ 20 nm
12	0.5 %	Toluene (RT)	Ag	4 h	~ 10 nm
13	1 %	Toluene (RT)	Ag	1.5 h	~ 8 nm
14	1 %	Toluene (RT)	Ag	1 h	~ 6 nm
15	1 %	Toluene (RT)	Ag	0.75 h	~ 6 nm

Table 6-1: APTES profiles for various binding conditions.

It has to be noted that APTES layer on Ag surface was characterized based on physical geometry of interest ($Ag/SiO_2/Ag$), and averaged roughness of MDM film (see Figure 6-7) was considered for characterization. The expected refractive index of small molecule

APTES was 1.46 [109] at the visible wavelength and uniform layer of film was formed on both Ag and SiO_2 surfaces.

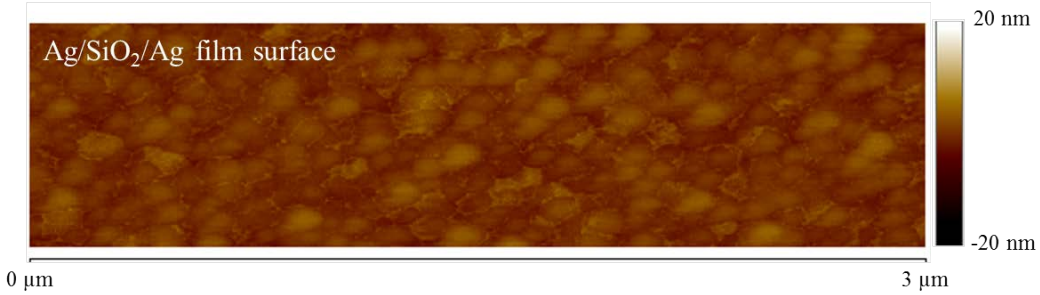

Figure 6-7: AFM image of $Ag/SiO_2/Ag$ film evaporated on BK7 glass. Averaged roughness of surface was about 1.8 nm.

In order to form a thin layer of APTES film on the proposed geometry in Figure 6-1, 1.0 % APTES solution in dry toluene was prepared at room temperature and the fabricated devices were immersed for various times in order to create different thickness of thin films. The expected film profile assembled on the geometry is shown in Figure 6-8(a) and its enlarged diagram is shown in Figure 6-8(b).

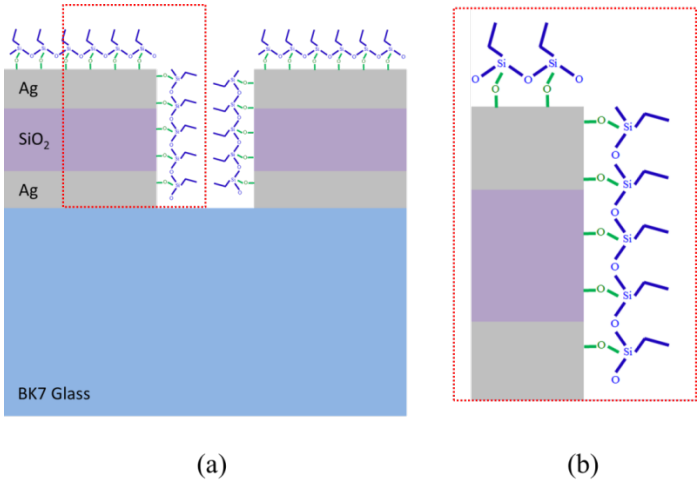

Figure 6-8: (a) Slit-gratings in MDM film coated with APTES. (b) Enlarged image of self-assembled APTES bond on Ag and SiO_2 surfaces.

After a self-assembled APTES layer was formed, the devices were cleaned by dipping in dry toluene at room temperature to remove APTES residues. Devices coated with different thickness of APTES film were prepared based on the Table 6-1 and then characterized under the microscope to see the intensity variations for various film thickness (see Figure 6-9).

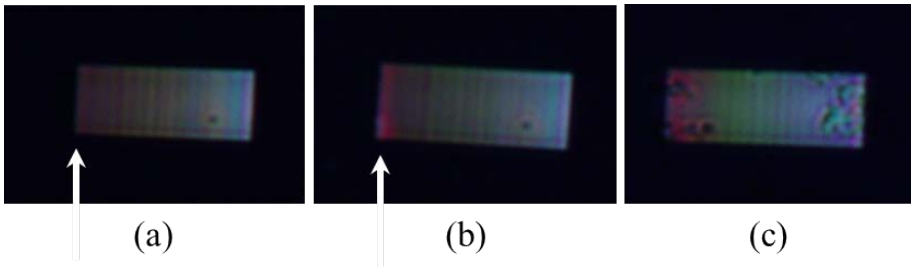

Figure 6-9: Microscope images of transmitted light for various thin APTES film thickness: images with (a) no APTES film, (b) 6 nm-thick APTES film, and (c) 30 nm-thick APTES film.

It is noticed that upon the presence of 6 nm-thick APTES film assembled on the geometry, the gratings with larger periodicity showed significant changes in transmission intensity as shown in Figure 6-9(b). Upon the presence of relatively thick APTES film (30 nm), transmission intensities from slit-gratings for various periodicity are enhanced. This enhanced transmission is related to tailoring impedance matching condition similar to that we saw in the tunable transmission with bulk index modification. Due to the presence of higher index especially inside slit-gratings, more efficient light transmission can occur with all grating periodicities.

6.5 CONCLUSIONS

It is seen how light transmission can be tailored by controlling bulk/local dielectric index. By tailoring the index of bulk medium surrounding the slit-gratings, we observed that the peak transmission spectrum can be tailored more than 40 nm for the index variation $\Delta n = 0.24$. Being based on the sharp transmission nature, specific colors transmitted through the proposed geometry with various grating periodicities are demonstrated.

Appendix A. Computer Codes

Mathematica codes for calculating transmission and reflection of slit-grating geometry is listed in the table below. Transmission-line (TL) approach is used to model the geometry in Figure 5-1.

```
nm = 10^-9; THz = 10^12;
(*0. Constitute Parameters for Silver film*)
  Subscript[\[Epsilon], 0] = 1/(36 \[Pi])*10^-9; Subscript[\[Mu], 0] =
  4 \[Pi]*10^-7; Subscript[\[Epsilon], \[Infinity]] = 5; Subscript[c, \
0] = 3*10^8;
(*1. Nateural Frequency of Electron Subscript[\[ScriptF], \
p]=2.175x10^15*)
Subscript[\[ScriptF], p] = 2.175*10^15;
(*2. Damping Constant \[Gamma]=4.35x10^12*)
\[Gamma] = 4.35*10^12;
(*3. Dispersion of complex Electric Susceptibility*)
\[Epsilon]m[
     f_] := (Subscript[\[Epsilon], \[Infinity]] - Subscript[\[ScriptF],
       p]^2/(f (f + I \[Gamma])))    ;
\[Lambda] = 633 nm;
<< PlotLegends`
Plot[{Re[\[Epsilon]m[f]], Im[\[Epsilon]m[f]]}, {f, 100 THz, 800 THz},
  PlotLegend -> {"\!\(\*SubscriptBox[\(\[Epsilon]\), \(m\)]\)\
\[CloseCurlyQuote]",
```

```
    "-\!\(\*SubscriptBox[\(\[Epsilon]\), \(m\)]\)\
\[CloseCurlyDoubleQuote]"}]
\[Lambda] = 630 nm; f = Subscript[c, 0]/\[Lambda]; \[Epsilon]m[f]
Subscript[w, s] = 50 nm; Subscript[w, g] =
  50 nm; Subscript[\[Epsilon], s] = 1; Subscript[\[Epsilon], g] = 1; \
Subscript[\[Eta], 0] = 120 \[Pi]; d =
  350 nm; l = (d)/2; Subscript[t, 1] = 50 nm; Subscript[t, 2] =
  50 nm; Subscript[t, 3] = 25 nm;
fmin = 10 THz; fmax = 800 THz;
k0[f_] := 2 \[Pi] f Sqrt[Subscript[\[Epsilon], 0] Subscript[\[Mu], 0]];
b[w_, f_, \[Epsilon]d_] :=
   b /. FindRoot[
      w/2 Sqrt[b^2 - \[Epsilon]d k0[f]^2] ==
        ArcTanh[-\[Epsilon]d/\[Epsilon]m[f] Sqrt[
           b^2 - \[Epsilon]m[f] k0[f]^2]/Sqrt[
           b^2 - \[Epsilon]d k0[
               f]^2]], {b, (2.23412312380000000000654684 + 0.00001 I)*
         k0[f]}];
ns = 800;
na = 2.5;
Res = Array[0 &, {na, ns}];
For[j = 0, j <= 2, j += 1, Subscript[\[Epsilon], s] = (j/10*1.5 + 1);
  \[Theta] = 0;
  \[Phi]f[f_] := (d)*k0[f]*Sin[\[Theta]];
  For[i = 1; xr = Array[# &, ns]; xt = Array[# &, ns];
```

```
tmp1 = Array[# &, ns]; tmp2 = Array[# &, ns]; tmp3 = Array[# &, ns];

  freq = Array[# &, ns]

, i <= ns , i += 1

, f = fmin + (fmax - fmin)*(i - 1)/(ns - 1);


ks = b[Subscript[w, s], f, Subscript[\[Epsilon], s]];

kg = b[Subscript[w, g], f, Subscript[\[Epsilon], g]];

ko = 2 \[Pi] f Sqrt[Subscript[\[Epsilon], 0] Subscript[\[Mu], 0]];

\[Omega] = 2 \[Pi] f;

\[Phi] = \[Phi]f[f];

Z0 = Subscript[\[Eta], 0] d Cos[\[Theta]];

Zs = Subscript[w, s]*ks/(\[Omega] Subscript[\[Epsilon], 0]);

Zg = Subscript[w, g]*kg/(\[Omega] Subscript[\[Epsilon], 0]);


\[Gamma]r[r_] := -((

    E^(I \[Phi]/2) (E^(I kg l) E^(I ks Subscript[w, s]))/(

       1 - E^(I \[Phi] ) E^(I kg d)) -

     r E^(-I \[Phi]/2) (E^(-I kg l) E^(-I ks Subscript[w, s]))/(

       1 - E^(-I \[Phi] ) E^(-I kg d)))/(

    E^(-I \[Phi]/2) (E^(I kg l) E^(I ks Subscript[w, s]))/(

       1 - E^(-I \[Phi] ) E^(I kg d)) -

     r E^(I \[Phi]/2) (E^(-I kg l) E^(-I ks Subscript[w, s]))/(

       1 - E^(I \[Phi] ) E^(-I kg d))));

\[Gamma]l[r_] := 1/\[Gamma]r[r];

ZLr[r_] := Zg*(1 + \[Gamma]r[r])/(1 - \[Gamma]r[r]);
```

```
ZLl[r_] := Zg*(1 + \[Gamma]l[r])/(1 - \[Gamma]l[r]);

ZL[r_] :=

  Zg*(ZLr[r] - I Zg*Tan[kg*l])/(Zg - I ZLr[r]*Tan[kg*l]) +

    Zg*(ZLl[r] - I Zg*Tan[kg*l])/(Zg - I ZLl[r]*Tan[kg*l]);



Tt1 = {{E^(-I ks Subscript[t, 1]), 0}, {0, E^(

     I ks Subscript[t, 1])}};

Tt2 = {{E^(-I ks Subscript[t, 2]), 0}, {0, E^(

     I ks Subscript[t, 2])}};


Tload[r_] := {{1 + ZL[r]/(2*Zs), ZL[r]/(2*Zs)}, {-(ZL[r]/(2*Zs)),

     1 - ZL[r]/(2*Zs)}};


T[r_] := Tt1.Tload[r].Tt2;

Tin = 1/

    2*{{Zs/Z0 +

         Zs*ks/(\[Omega] Subscript[\[Mu], 0] Subscript[w, s]), -(Zs/

           Z0) + Zs*

           ks/(\[Omega] Subscript[\[Mu], 0] Subscript[w, s])}, {-(Zs/

           Z0) + Zs*ks/(\[Omega] Subscript[\[Mu], 0] Subscript[w, s]),

        Zs/Z0 + Zs*ks/(\[Omega] Subscript[\[Mu], 0] Subscript[w, s])}};

  "Tout= \!\(\*FractionBox[\(1\), \

\(2\)]\)\[Times]{{\!\(\*FractionBox[\(Z0\), \

\(Zs\)]\)+Z0\[Times]\!\(\*FractionBox[\(ko\), \(\[Omega]\\\ \
```

```
\*SubscriptBox[\(\[Mu]\), \(0\)]\\\ d\)]\),-\!\(\*FractionBox[\(Z0\), \
\(Zs\)]\)+Z0\[Times]\!\(\*FractionBox[\(ko\), \(\[Omega]\\\ \
\*SubscriptBox[\(\[Mu]\), \(0\)]\\\ \
d\)]\)},{-\!\(\*FractionBox[\(Z0\), \
\(Zs\)]\)+Z0\[Times]\!\(\*FractionBox[\(ko\), \(\[Omega]\\\ \
\*SubscriptBox[\(\[Mu]\), \(0\)]\\\ d\)]\),\!\(\*FractionBox[\(Z0\), \
\(Zs\)]\)+Z0\[Times]\!\(\*FractionBox[\(ko\), \(\[Omega]\\\ \
\*SubscriptBox[\(\[Mu]\), \(0\)]\\\ d\)]\)}};";
    Tout = PseudoInverse[Tin, Tolerance -> 0];
    M[r_] := T[r];


    tmpM[r_] := Tin.M[r].Tout;
    funT[r_] := 1/tmpM[r][[1]][[1]];
    freq[[i]] = f;


    ref = r /. FindRoot[funT[r]*tmpM[r][[2]][[1]] == r, {r, 0.001 I}];
    tmpm = tmpM[ref];
    xr[[i]] = ref;
    xt[[i]] = funT[ref];
    ];


  Res[[j + 1]] = Abs[xt]^2;
  ]
Xt = Transpose[{freq, Abs[xt]}];
Xr = Transpose[{freq, Abs[xr]}];
```

```
ListLinePlot[Xr]

ListLinePlot[Xt]

ListDensityPlot[Res]

Export["Result.xls", Res, "Table"];
```

References

1. Maxwell, J.C., *A Dynamical Theory of the Electromagnetic Field.* Philosophical Transactions of the Royal Society of London, 1865. **155**: p. 459-512.
2. Ronchi, V., *Forty Years of History of a Grating Interferometer.* Applied Optics, 1964. **3**(4): p. 437-451.
3. Boivin, L., *Multiple imaging using various types of simple phase gratings.* Applied optics, 1972. **11**(8): p. 1782-1792.
4. Fraunhofer, J., *Kurzer Bericht von den Resultaten neuerer Versuche über die Gesetze des Lichtes, und die Theorie derselben.* Annalen der Physik, 1823. **74**(8): p. 337-378.
5. Hoose, J. and E. Popov, *Two-dimensional gratings for low polarization dependent wavelength demultiplexing.* Applied optics, 2008. **47**(25): p. 4574-4578.
6. Hopkinson, F. and D. Rittenhouse, *An optical problem, proposed by Mr. Hopkinson, and solved by Mr. Rittenhouse.* Transactions of the American Philosophical Society, 1786. **2**: p. 201-206.
7. Knop, K., *Diffraction gratings for color filtering in the zero diffraction order.* Applied optics, 1978. **17**(22): p. 3598-3603.
8. Loewen, E.G. and E. Popov, *Diffraction gratings and applications*. 1997: CRC Press.
9. Mashev, L. and E. Popov, *Zero order anomaly of dielectric coated gratings.* Optics communications, 1985. **55**(6): p. 377-380.
10. Moharam, M.G. and T.K. Gaylord, *Rigorous coupled-wave analysis of planar-grating diffraction.* Journal of the Optical Society of America, 1981. **71**(7): p. 811-818.
11. Moharam, M.G. and T.K. Gaylord, *Rigorous coupled-wave analysis of grating diffraction?E-mode polarization and losses.* Journal of the Optical Society of America, 1983. **73**(4): p. 451-455.
12. Moharam, M.G. and T.K. Gaylord, *Three-dimensional vector coupled-wave analysis of planar-grating diffraction.* Journal of the Optical Society of America, 1983. **73**(9): p. 1105-1112.
13. Newton, I., *A new theory about light and colors.* American journal of physics, 1993. **61**(2): p. 108-112.
14. Popov, E., L. Mashev, and D. Maystre, *Theoretical study of the anomalies of coated dielectric gratings.* Journal of Modern Optics, 1986. **33**(5): p. 607-619.
15. Tibuleac, S. and R. Magnusson, *Narrow-linewidth bandpass filters with diffractive thin-film layers.* Optics letters, 2001. **26**(9): p. 584-586.
16. Wang, S., et al., *Guided-mode resonances in planar dielectric-layer diffraction gratings.* JOSA A, 1990. **7**(8): p. 1470-1474.

17. Wang, S.S. and R. Magnusson, *Design of waveguide-grating filters with symmetrical line shapes and low sidebands.* Optics Letters, 1994. **19**(12): p. 919-921.
18. Wenger, J., et al., *Biophotonics applications of nanometric apertures.* International Journal of Materials and Product Technology, 2009. **34**(4): p. 488-506.
19. Wood, R.W., *On a Remarkable Case of Uneven Distribution of Light in a Diffraction Grating Spectrum.* Proceedings of the Physical Society of London, 1902. **18**(1): p. 269.
20. Fano, U., *The Theory of Anomalous Diffraction Gratings and of Quasi-Stationary Waves on Metallic Surfaces (Sommerfeld?s Waves).* Journal of the Optical Society of America, 1941. **31**(3): p. 213-222.
21. Hessel, A. and A.A. Oliner, *A New Theory of Wood's Anomalies on Optical Gratings.* Applied Optics., 1965. **4**(10): p. 1275-1297.
22. Rayleigh, L., *III. Note on the remarkable case of diffraction spectra described by Prof. Wood.* Philosophical Magazine Series 6, 1907. **14**(79): p. 60-65.
23. Twersky, V., *Multiple Scattering of Waves and Optical Phenomena.* Journal of the Optical Society of America, 1962. **52**(2): p. 145-169.
24. Ashbaugh, M.S. and R.D. Benguria, *On Rayleigh's conjecture for the clamped plate and its generalization to three dimensions.* 1995: p. 1-17.
25. Deplazes, A. and A.k. Moravánszky, *1:1 Wood Works : ein experimenteller Massivbau*. 2003, Zürich: gta Verlag. 48 p.
26. Rayleigh, L., *On the Dynamical Theory of Gratings.* Proceedings of the Royal Society of London. Series A, Containing Papers of a Mathematical and Physical Character, 1907. **79**(532): p. 399-416.
27. Magnusson, R. and T.K. Gaylord, *Analysis of multiwave diffraction of thick gratings.* Journal of the Optical Society of America, 1977. **67**(9): p. 1165-1170.
28. Maystre, D., *Sur la diffraction d'une onde plane par un reseau metallique de conductivite finie.* Optics Communications, 1972. **6**(1): p. 50-54.
29. Maystre, D., *Sur la diffraction d'une onde plane electromagnetique par un reseau metallique.* Optics Communications, 1973. **8**(3): p. 216-219.
30. Parthasarathy, S., *Diffraction of light by ultrasonic waves.* Proceedings of the Indian Academy of Sciences - Section A, 1936. **3**(5): p. 442-447.
31. Phariseau, P., *On the diffraction of light by progressive supersonic waves.* Proceedings of the Indian Academy of Sciences - Section A, 1956. **44**(4): p. 165-170.
32. Fillmore, G.L. and R.F. Tynan, *Sensitometric Characteristics of Hardened Dichromated-Gelatin Films.* Journal of the Optical Society of America, 1971. **61**(2): p. 199-203.
33. Case, S.K., *Coupled-wave theory for multiply exposed thick holographic gratings.* Journal of the Optical Society of America, 1975. **65**(6): p. 724-729.
34. Kong, J.A., *Second-order coupled-mode equations for spatially periodic media.* Journal of the Optical Society of America, 1977. **67**(6): p. 825-829.

35. Tamir, T., *Scattering of electromagnetic waves by a sinusoidally stratified half-space: ii. diffraction aspects at the rayleigh and bragg wavelengths.* Canadian Journal of Physics, 1966. **44**(10): p. 2461-2494.
36. Tamir, T. and H.C. Wang, *Scattering of electromagnetic waves by a sinusoidally stratified half-space: ii. diffraction aspects at the rayleigh and bragg wavelengths.* Canadian Journal of Physics, 1966. **44**(9): p. 2073-2094.
37. Tamir, T., H.C. Wang, and A.A. Oliner, *Wave Propagation in Sinusoidally Stratified Dielectric Media.* Microwave Theory and Techniques, IEEE Transactions on, 1964. **12**(3): p. 323-335.
38. Burckhardt, C.B., *Diffraction of a Plane Wave at a Sinusoidally Stratified Dielectric Grating.* Journal of the Optical Society of America, 1966. **56**(11): p. 1502-1508.
39. Ruey-Shi, C. and T. Tamir, *Guided-Wave Theory of Light Diffraction by Acoustic Microwaves.* Microwave Theory and Techniques, IEEE Transactions on, 1970. **18**(8): p. 486-504.
40. Chu, R.S. and T. Tamir, *Wave propagation and dispersion in space-time periodic media.* Electrical Engineers, Proceedings of the Institution of, 1972. **119**(7): p. 797-806.
41. Kaspar, F.G., *Diffraction by thick, periodically stratified gratings with complex dielectric constant.* Journal of the Optical Society of America, 1973. **63**(1): p. 37-45.
42. Ruey-Shi, C. and K. Jin Au, *Modal Theory of Spatially Periodic Media.* Microwave Theory and Techniques, IEEE Transactions on, 1977. **25**(1): p. 18-24.
43. Norton, K., *The propagation of radio waves over the surface of the earth and in the upper atmosphere*. Radio Engineers, Proceedings of the Institute of, 1936. **24**(10): p. 1367-1387.
44. Sommerfeld, A., *Über die Ausbreitung der Wellen in der drahtlosen Telegraphie.* Annalen der Physik, 1909. **333**(4): p. 665-736.
45. Mie, G., *Beiträge zur Optik trüber Medien, speziell kolloidaler Metallösungen.* Annalen der Physik, 1908. **330**(3): p. 377-445.
46. Gans, R., *Über die Form ultramikroskopischer Goldteilchen.* Annalen der Physik, 1912. **342**(5): p. 881-900.
47. Ghosh, E.D.P.a.G., *Handbook of Optical Constants of Solids*. 1st ed. 1997, Orlando, FL: Academic PRESS.
48. Lee, Y., et al., *Efficient directional beaming from small apertures using surface-plasmon diffraction gratings.* Applied Physcis Letter, 2012. **101**(4): p. 041102.
49. P. Lalanne, J.P.H., and J. C. Rodier, *Theory of Surface Plasmon Generation at Nanoslit Apertures.* Physical Review Letter, 2005. **95**: p. 263902.
50. Johnson, P.B. and R.W. Christy, *Optical Constants of the Noble Metals.* Physical Review B, 1972. **6**(12): p. 4370-4379.
51. Medina, F., F. Mesa, and R. Marques, *Extraordinary Transmission Through Arrays of Electrically Small Holes From a Circuit Theory Perspective.*

Microwave Theory and Techniques, IEEE Transactions on, 2008. **56**(12): p. 3108-3120.
52. Medina, F., F. Mesa, and R. Marques. *Equivalent circuit model to explain extraordinary transmission*. in *Microwave Symposium Digest, 2008 IEEE MTT-S International*. 2008.
53. T. W. Ebbesen, H.J.L., H. F. Ghaemi, T. Thio, and P. A. Wolff, *Extraordinary optical transmission through sub-wavelength hole arrays.* Letters to Nature, 1998. **391**: p. 667-669.
54. Pincemin, F., et al., *Scattering of a surface plasmon polariton by a surface defect.* Physical Review Letter B, 1994. **50**(20): p. 15261-15275.
55. Chen, P., et al., *Near-Field-Resonance-Enhanced Plasmonic Light Beaming.* Photonics Journal, IEEE, 2010. **2**(1): p. 8-17.
56. Hao, F., R. Wang, and J. Wang, *A design methodology for directional beaming control by metal slit–grooves structure.* Journal of Optics, 2011. **13**(1): p. 015002.
57. Kim, H., J. Park, and B. Lee, *Tunable directional beaming from subwavelength metal slits with metal?dielectric composite surface gratings.* Optics Letter, 2009. **34**(17): p. 2569-2571.
58. Kim, S., et al., *Off-axis directional beaming of optical field diffracted by a single subwavelength metal slit with asymmetric dielectric surface gratings.* Applied Physics Letters, 2007. **90**(5): p. 051113.
59. Lezec, H.J., et al., *Beaming Light from a Subwavelength Aperture.* Science, 2002. **297**(5582): p. 820-822.
60. Kim, H. and B. Lee, *Unidirectional Surface Plasmon Polariton Excitation on Single Slit with Oblique Backside Illumination.* Plasmonics, 2009. **4**(2): p. 153-159.
61. Lee, Y., A. Alu, and X.J. Zhang, *Efficient apertureless scanning probes using patterned plasmonic surfaces.* Optics Express, 2011. **19**(27): p. 25990-25999.
62. Ferry, V.E., et al., *Plasmonic Nanostructure Design for Efficient Light Coupling into Solar Cells.* Nano Letters, 2008. **8**(12): p. 4391-4397.
63. *PAVE PAWS RADAR SYSTEM*. Available from: http://www.afspc.af.mil/library/factsheets/factsheet.asp?id=3656.
64. *AN/APG-77 Radar System*. Available from: http://www.globalsecurity.org/military/systems/aircraft/systems/an-apg-77.htm.
65. Li, J., A. Salandrino, and N. Engheta, *Shaping light beams in the nanometer scale: A Yagi-Uda nanoantenna in the optical domain.* Physical Review B, 2007. **76**(24): p. 245403.
66. Kosako, T., Y. Kadoya, and H.F. Hofmann, *Directional control of light by a nano-optical Yagi-Uda antenna.* Nat Photon, 2010. **4**(5): p. 312-315.
67. Curto, A.G., et al., *Unidirectional Emission of a Quantum Dot Coupled to a Nanoantenna.* Science, 2010. **329**(5994): p. 930-933.
68. Holger, F.H., K. Terukazu, and K. Yutaka, *Design parameters for a nano-optical Yagi–Uda antenna.* New Journal of Physics, 2007. **9**(7): p. 217.

69. Taminiau, T.H., F.D. Stefani, and N.F. van Hulst, *Enhanced directional excitation and emission of single emitters by a nano-optical Yagi-Uda antenna.* Optics Express, 2008. **16**(14): p. 10858-10866.
70. Pellegrini, G., G. Mattei, and P. Mazzoldi, *Tunable, directional and wavelength selective plasmonic nanoantenna arrays.* Nanotechnology, 2009. **20**(6): p. 065201.
71. Koenderink, A.F., *Plasmon Nanoparticle Array Waveguides for Single Photon and Single Plasmon Sources.* Nano Letters, 2009. **9**(12): p. 4228-4233.
72. Coenen, T., et al., *Directional Emission from Plasmonic Yagi–Uda Antennas Probed by Angle-Resolved Cathodoluminescence Spectroscopy*. Nano Letters, 2011. **11**(9): p. 3779-3784.
73. Liu, X.-X. and A. Alù, *Subwavelength leaky-wave optical nanoantennas: Directive radiation from linear arrays of plasmonic nanoparticles.* Physical Review B, 2010. **82**(14): p. 144305.
74. Kim, S., et al., *Optical beam focusing by a single subwavelength metal slit surrounded by chirped dielectric surface gratings.* Applied Physics Letters, 2008. **92**(1): p. 013103.
75. Oliner, A.A. and D.R. Jackson, *Antenna Engineering Handbook*. 4th ed. 2007, New York: McGraw-Hill.
76. Balanis, C.A., *Antenna Theory Analysis and Design*. 2005, New Jersey: John Wiley & Sons.
77. Logeeswaran, V.J., et al., *Ultrasmooth Silver Thin Films Deposited with a Germanium Nucleation Layer.* Nano Letters, 2008. **9**(1): p. 178-182.
78. J-Y Laluet, A.D., C Genet and T W Ebbesen, *Generation of surface plasmons at single subwavelength slits: from slit to ridge plasmon.* New Journal of Physics, 2008. **10**: p. 105014.
79. Lalanne, P. and J.P. Hugonin, *Interaction between optical nano-objects at metallo-dielectric interfaces.* Nature Physics, 2006. **2**(8): p. 551-556.
80. Qiaoqiang Gan, Y.G., 1 Qing Wang,2 Lin Zhu,3 and Filbert Bartoli1,*, *Surface plasmon waves generated by nanogrooves through spectral interference.* Physical Review B, 2010. **81**: p. 085443.
81. Kretschmann, E. and H. Räther, *Radiative decay of nonradiative surface plasmon excited by light.* Zeitung für Naturforschung, 1968. **23A**: p. 2135-2136.
82. Neviere, M., R. Petit, and M. Cadilhac, *About the theory of optical grating coupler-waveguide systems.* Optics Communications, 1973. **8**(2): p. 113-117.
83. Neviere, M., et al., *Systematic study of resonances of holographic thin film couplers.* Optics Communications, 1973. **9**(1): p. 48-53.
84. Peng, S. and G.M. Morris, *Resonant scattering from two-dimensional gratings.* Journal of the Optical Society of America A, 1996. **13**(5): p. 993-1005.
85. Taubert, R., et al., *Octave-wide photonic band gap in three-dimensional plasmonic Bragg structures and limitations of radiative coupling.* Nature Communications, 2012. **3**: p. 691.

86. Zhou, W. and T.W. Odom, *Tunable subradiant lattice plasmons by out-of-plane dipolar interactions.* Nature Nano, 2011. **6**(7): p. 423-427.
87. Agio, M. and A. Alù, *Optical antennas*.
88. Auguié, B. and W.L. Barnes, *Collective Resonances in Gold Nanoparticle Arrays.* Physical Review Letters 2008. **101**(14): p. 143902.
89. Adato, R., et al., *Radiative engineering of plasmon lifetimes in embedded nanoantenna arrays.* Optical Express, 2010. **18**(5): p. 4526-4537.
90. Husaini, S., L. Deych, and V.M. Menon, *Plasmon-resonance-induced enhancement of the reflection band in a one-dimensional metal nanocomposite photonic crystal.* Optics Letter. 2011. **36**(8): p. 1368-1370.
91. Li, P.-C. and E.T. Yu, *Wide-angle wavelength-selective multilayer optical metasurfaces robust to interlayer misalignment.* Journal of the Optical Society of America B, 2013. **30**(1): p. 27-32.
92. Rizzi, P.A., *Microwave Filters Utilizing the Cutoff Effect.* Microwave Theory and Techniques, IRE Transactions on, 1956. **4**(1): p. 36-40.
93. Andrea Alù, N.E., *Optical nanotransmission lines: synthesis of planar left-handed metamaterials in the infrared and visible regimes.* Journal of Optical Society of America B, 2006. **23**.
94. García de Abajo, F.J., *Colloquium: Light scattering by particle and hole arrays.* Reviews of Modern Physics, 2007. **79**(4): p. 1267-1290.
95. Alù, A., et al., *Plasmonic Brewster Angle: Broadband Extraordinary Transmission through Optical Gratings.* Physical Review Letters, 2011. **106**(12): p. 123902.
96. A. Alù, a.N.E., *Structured Surfaces as Optical Metamaterials*. 2011, Cambridge University Press.
97. Chen, W., et al., *Ultra-thin ultra-smooth and low-loss silver films on a germanium wetting layer.* Optics Express, 2010. **18**(5): p. 5124-5134.
98. Sozo Yokogawa, ‡,§ Stanley P. Burgos,†,§ and Harry A. Atwater*,†, *Plasmonic Color Filters for CMOS Image Sensor Applications.* Nano Letters, 2012. **12**(4349-4354).
99. Tal Ellenbogen *, K.S., and Kenneth B. Crozier *, *Chromatic Plasmonic Polarizers for Active Visible Color Filtering and Polarimetry*. Nano Letters, 2012. **12**(2): p. 1026-1031.
100. Ting Xu, Y.-K.W., Xiangang Luo, and L. Jay Guo, *Plasmonic nanoresonators for high-resolution colour fi ltering and spectral imaging.* Nature Communications, 2010.
101. Asanka Pannipitiya, ∗ Ivan D. Rukhlenko,1 Malin Premaratne,1 and a.G.P.A. Haroldo T. Hattori, *Improved transmission model for metal-dielectric-metal plasmonicwaveguides with stub structure*. Optics Express, 2010. **18**.
102. Fan, G.V.a.S., *Bends and splitters in metal-dielectric-metal subwavelength plasmonic waveguides.* Applied Physcis Letter, 2005. **87**.
103. Huang, X.L.a.X., *Numerical modeling of a teeth-shaped nanoplasmonic waveguide filter.* Journal of Optical Society of America B, 2009. **26**.

104. Jianlong Liu1, G.F., Haifa Zhao1,Yan Zhang2, Shutian and Liu1, *Surface plasmon reflector based on serial stub structure.* Optics Express, 2009. **17**(22): p. 20134-20139.
105. Yousuke Matsuzaki, T.O., Masanobu Haraguchi, Masuo Fukui, and Masatoshi Nakagaki *Characteristics of gap plasmon waveguide with stub structures.* Optics Express, 2008. **16**(21): p. 16314-16325
106. Lv, Y., et al., *Antibiotic glass slide coated with silver nanoparticles and its antimicrobial capabilities.* Polymers for Advanced Technologies, 2008. **19**(11): p. 1455-1460.
107. Lv, Y., et al., *Silver nanoparticle-decorated porous ceramic composite for water treatment.* Journal of Membrane Science, 2009. **331**(1–2): p. 50-56.
108. Sidorov, A.N., et al., *A surface-enhanced Raman spectroscopy study of thin graphene sheets functionalized with gold and silver nanostructures by seed-mediated growth.* Carbon, 2012. **50**(2): p. 699-705.
109. Ouyang, H., et al., *Macroporous Silicon Microcavities for Macromolecule Detection.* Advanced Functional Materials, 2005. **15**(11): p. 1851-1859.